Mechanisms of generation of membrane potential resonance in a neuron with multiple resonant ionic currents

David M. Fox[1], Hua-an Tseng[1,#a], Tomasz G. Smolinski[2], Horacio G. Rotstein[3,1,¶] and Farzan Nadim[1,3*,¶]

1. Federated Department of Biological Sciences, New Jersey Institute of Technology and Rutgers University-Newark, Newark, NJ, USA
2. Department of Computer and Information Sciences, Delaware State University, Dover, DE, USA
3. Department of Mathematical Sciences, New Jersey Institute of Technology, Newark, NJ, USA

[#a] H-a Tseng's present address: Department of Biomedical Engineering, Boston University, Boston, MA, USA

*Corresponding author:
e-mail: farzan@njit.edu

[¶] These authors contributed equally to this work.

Keywords:
Preferred frequency response; stomatogastric; model neuron, evolutionary algorithm, oscillations

Abstract

Neuronal membrane potential resonance (MPR) is associated with subthreshold and network oscillations. A number of voltage-gated ionic currents can contribute to the generation or amplification of MPR, but how the interaction of these currents with linear currents contributes to MPR is not well understood. We explored this in the pacemaker PD neurons of the crab pyloric network. The PD neuron MPR is sensitive to blockers of H- (I_H) and calcium-currents (I_{Ca}). We used the impedance profile of the biological PD neuron, measured in voltage clamp, to constrain parameter values of a conductance-based model using a genetic algorithm and obtained many optimal parameter combinations. Unlike most cases of MPR, in these optimal models, the values of resonant- (f_{res}) and phasonant- ($f_{\varphi=0}$) frequencies were almost identical. Taking advantage of this fact, we linked the peak phase of ionic currents to their amplitude, in order to provide a mechanistic explanation the dependence of MPR on the I_{Ca} gating variable time constants. Additionally, we found that distinct pairwise correlations between I_{Ca} parameters contributed to the maintenance of f_{res} and resonance power (Q_Z). Measurements of the PD neuron MPR at more hyperpolarized voltages resulted in a reduction of f_{res} but no change in Q_Z. Constraining the optimal models using these data unmasked a positive correlation between the maximal conductances of I_H and I_{Ca}. Thus, although I_H is not necessary for MPR in this neuron type, it contributes indirectly by constraining the parameters of I_{Ca}.

Author Summary

Many neuron types exhibit membrane potential resonance (MPR) in which the neuron produces the largest response to oscillatory input at some preferred (resonant) frequency and, in many systems, the network frequency is correlated with neuronal MPR. MPR is captured by a peak in the impedance vs. frequency curve (Z-profile), which is shaped by the dynamics of voltage-gated ionic currents. Although neuron types can express variable levels of ionic currents, they may have a stable resonant frequency. We used the PD neuron of the crab pyloric network to understand how MPR emerges from the interplay of the biophysical properties of multiple ionic currents, each capable of generating resonance. We show the contribution of an inactivating current at the resonant frequency in terms of interacting time constants. We measured the Z-profile of the PD neuron and explored possible combinations of model parameters that fit this experimentally measured profile. We found that the Z-profile constrains and defines correlations among parameters associated with ionic currents. Furthermore, the resonant frequency and amplitude are sensitive to different parameter sets and can be preserved by co-varying pairs of parameters along their correlation lines. Furthermore, although a resonant current may be present in a neuron, it may not directly contribute to MPR, but constrain the properties of other currents that generate MPR. Finally, constraining model parameters further to those that modify their MPR properties to changes in voltage range produces maximal conductance correlations.

Introduction

Neuronal network oscillations at characteristic frequency bands emerge from the coordinated activity of the participating neurons. Membrane potential resonance (MPR) is defined as the ability of neurons to exhibit a peak in their voltage response to oscillatory current inputs at a preferred or resonant frequency (f_{res}) [1]. MPR has been observed in many neuron types such as those in the hippocampus [2-4] and entorhinal cortex [2-6], inferior olive [7, 8], thalamus [1, 9], striatum [10, 11], as well as in invertebrate oscillatory networks such as the pyloric network of the crustacean stomatogastric ganglion (STG) [12-14]. Neurons may also exhibit phasonance or a zero-phase response, which describes their ability to synchronize with oscillatory inputs at a preferred phasonant frequency ($f_{\varphi=0}$) [4, 15-18]. Resonance, phasonance and intrinsic oscillations are related, but are different phenomena as one or more of them may be present in the absence of the others [15, 16, 18].

Resonant and phasonant frequencies result from a combination of low- and high-pass filter mechanisms produced by the interplay of the neuron's passive properties and one or more ionic currents and their interaction with the oscillatory inputs [1, 15, 18, 19]. The slow resonant currents (or currents having resonant gating variables) oppose voltage changes and act as high-pass filters. They include the hyperpolarization-activated inward current (I_H) and the slow outward potassium current (I_M). On the other hand, the fast amplifying currents (or currents having amplifying gating variables) favor voltage changes and can make MPR more pronounced. They include the persistent sodium current (I_{NaP}) and the inward rectifying potassium (I_{Kir}) current. Most previous systematic mechanistic studies have primarily examined models with one resonant and one amplifying current, such as I_H and I_{NaP}, respectively [15, 18-20]. Currents having both activating and inactivating gating variables (in a multiplicative way) such as the low-threshold calcium current (I_{Ca}) are not included in this classification, but they are able to produce resonance by mechanisms that are less understood [16, 21].

Although a causal relationship between the properties of MPR and network activity has not been established [but see 22], resonant neurons have been implicated in the generation of network oscillations in a given frequency band because the resonant and network frequencies often match up or are correlated. One example is in the hippocampal theta oscillations [23] in which CA1 pyramidal cells exhibit MPR *in vitro* at theta frequencies of 4-10 Hz [2-4, 24] (but see [25]). Interestingly, MPR is not constant across the somatodendritic arbor in these neurons [26]. Hippocampal interneurons also show MPR *in vitro*, but at gamma frequencies of 30-50 Hz [3, but see 4], and gamma oscillations have been found to be particularly robust in network models containing resonant interneurons [27, 28].

The crab pyloric network produces stable oscillations at a frequency of ~1 Hz, driven by a pacemaker group composed of two neuron types, the anterior burster (AB) and the pyloric dilator (PD), that produce synchronized bursting oscillations through strong electrical-coupling [29]. The PD neuron shows MPR, with f_{res} ~1 Hz that is positively correlated with the pyloric network frequency [12]. Previous work has demonstrated that MPR in this neuron depends on two voltage-gated currents: I_{Ca} and I_H [12]. Ionic current levels in pyloric neurons are highly variable across animals, even in the same cell type [30]. It is therefore unclear how these currents may interact to produce a stable MPR in the PD neuron and whether this variability persists or is increased or decreased in the presence of oscillatory inputs.

Traditionally, MPR is measured by applying ZAP current injection and recording the amplitude of the voltage response [1, 31]. In some systems, depolarization can increase [32] or decrease [33], 1996) the preferred frequency. Alternatively, resonance is measured by applying ZAP voltage inputs in voltage clamp and recording the amplitude of the total current. Both approaches yield identical results for linear systems, but not necessarily for nonlinear systems. A previous study from our lab using the voltage clamp technique showed that in the PD neuron hyperpolarization decreases both f_{res} and network frequencies [14]. Since MPR results from the outcome of the dynamics of voltage-gated ionic currents activated in different voltage ranges, changing the input voltage amplitude is expected to change f_{res} in an input amplitude-dependent manner. This cannot be captured by linear models in which impedance is independent of the input amplitude. To our knowledge, no study has attempted to understand the ionic mechanisms that produce shifts in f_{res} in response to changes in the voltage range.

Previous studies have explored the generation of MPR by I_{Ca} and through the interaction between I_{Ca} and I_H in hippocampal CA1 pyramidal neurons [16, 17] and thalamic neurons [21], where the resonant and network frequencies are significantly higher than in the crab pyloric network and the I_{Ca} time constants are smaller. Based on numerical simulations, these investigations have produced important results about the role of the activating and inactivating gating variables and their respective time constants play in the generation of MPR and the determination of f_{res}. However, a mechanistic understanding of the effects of the interacting time constants and voltage-dependent inactivation that goes beyond simulations is lacking. An important finding for the CA1 pyramidal neurons is that, for physiological time constants, they exhibit resonance, but no phasonance [16]. However, for larger time constants, outside the physiological range for these neurons, they are able to exhibit phasonance. This suggests that PD neurons, which have slower time scale currents, may exhibit resonance and phasonance at comparable frequencies. If so, such a correlation between resonance and phasonance can be used to explain the influence of ionic current parameters.

Our study has two interconnected goals: (i) to understand how the interplay of multiple resonant gating variables shapes the Z- and ϕ-profiles (impedance amplitude and phase-shift as a function of input frequency) of a biological PD neuron, and (ii) to understand the many ways in which these interactions can occur to produce the same Z-profile in these neurons. For a neuron behaving linearly, e.g., with small subthreshold inputs, this task is somewhat simplified by the fact that linear components are additive. However, neurons are nonlinear and the nonlinear interaction between ionic currents has been shown to produce unexpected results [16, 18, 19].

To achieve these goals we measured and quantified the Z- and ϕ-profiles of the PD neuron. We then used a single-compartment conductance-based model of Hodgkin-Huxley type [34] that included a passive leak and the two voltage-gated currents I_H and I_{Ca} to explore what combinations of model parameters can produce the experimentally observed PD neuron Z- and ϕ-profiles. The maximal conductances of ionic currents of neurons in the stomatogastric nervous system vary widely [35-37]. We therefore assume that the parameters that determine the Z-profile in the PD neuron vary across animals. Thus, instead of searching for a single model that fit the PD neuron Z-profile, we used a genetic algorithm to capture a collection of parameter sets that fit this Z-profile. To achieve such a fit, we defined a set of ten attributes that characterize the PD neuron Z-profile (e.g., resonant frequency and amplitude) and used a multi-objective evolutionary algorithm [MOEA, 38] to obtain a family of models that fit these attributes. We then used this family of optimal models to identify the important biophysical parameters and relationships among these parameters to explain how the PD neuron Z-profile is shaped. We show how the fact that the inactivating calcium current peaks at the same phase as the passive properties, in response to sinusoidal inputs, can explain why resonant and phasonant frequencies are equal. We identify significant pairwise parameter-correlations, which selectively set certain attributes of MPR. We show that, in this neuron, I_H does not produce MPR but can extend the dynamic range of I_{Ca} parameters mediating MPR. Furthermore, we identify a subset of models that capture the experimental shift in the resonant frequency with changes in lower bound of voltage oscillation. Finally, we exploit the fact that the resonant and phasonant frequencies are equal for the PD neuron to provide a mechanistic understanding of the effects of the I_{Ca} time constants on the resonant frequency by using phase information. Our results provide a mechanistic understanding for a generic class of neurons that exhibit both resonance and phasonance as the result of the interaction between multiplicative gating variables and complement the studies in [16].

Results

The PD neuron produces 1 Hz bursting oscillations with a slow-wave approximately -60mV to -30mV (fig 3a). Driving the neuron through this voltage range with a ZAP function in voltage clamp (fig 3b top panel) produces a minimum (arrow in fig 3b bottom panel) in the amplitude of the current response (fig 3b). The input frequency at which this minimum occurs corresponds to a peak in the *Z*-profile (f_{res}, Z_{max}; fig 3c1). The value of f_{res} was 0.86 ± 0.05Hz producing Z_{max} values of 10.23 ± 0.51 MΩ (N = 18; fig 3d). The φ-profile shows a phasonant frequency $f_{\varphi=0}$ = 0.81 ± 0.05Hz, which in most cases matched f_{res} (fig 3c2). The PD neuron had a Q_Z of 2.77 ± 0.71 MΩ and $\Lambda_{½}$ of 0.53 ± 0.04 Hz. Across preparations, Q_Z showed considerable variability, whereas f_{res}, $\Lambda_{½}$, and $f_{\varphi=0}$ were relatively consistent (fig 3d). The corresponding median values for f_{res}, Q_Z, $\Lambda_{½}$, and $f_{\varphi=0}$ were 0.83 Hz, 2.77 MΩ, 0.5 Hz, 0.79 Hz, respectively.

To obtain model parameter combinations constrained by the PD neuron *Z*- and ϕ - profiles, we generated a population of models using an NSGA-II algorithm (see Methods). The attributes of a single PD neuron *Z*- and ϕ -profiles (fig 4, filled red circles) constrained the optimization of the parameter values. This resulted in a population of ~9000 sets of parameters ("optimal" dataset). All models in the optimal dataset captured the attributes of *Z* and ϕ to within 5% of the target (light blue lines in fig 4), with the exception of φ_{max}, which may be due to the anatomical structure of the PD neuron, a property that is omitted in our single-compartment model, or due to additional ionic currents, such as the potassium A current, which are not included in our model [16, 39].

The generation of MPR by the interaction of two resonant voltage-gated currents

To understand how *Z* is generated by the dynamics of individual ionic currents at different voltages and frequencies, we examined the amplitude and kinetics of ionic currents. In voltage clamp, *Z* is shaped by active voltage-gated currents, interacting with the passive leak and capacitive currents, in response to the voltage inputs. To understand the contribution of different ionic currents, we measured these currents in response to a constant frequency sine wave voltage inputs (fig 5a inset) at three frequencies: 0.1Hz, 1Hz (f_{res}) and 4Hz (fig 5). For these frequencies, we plotted the steady-state current as a function of voltage (fig 5b-d left) and normalized time (or cycle phase = time x frequency; fig 5b-d right). At 0.1 Hz, the amplitudes of I_H and I_L +I_{Cm} sets I_{total} at low (~ -60 mV) and high (~ -30 mV) voltages, respectively (fig 5b left). Since I_H deactivation is slow, it also contributes to I_{total} at high voltages (fig 5b right). At 1 Hz

(= f_{res}), I_H still sets the minimum of the total current, but, because of its slow kinetics, its steady-state dynamics are mostly linear (fig 5c left). However, now I_{Ca} peaks in phase (fig 5c right) with the passive I_L + I_{Cm} at high voltages, thus producing a smaller I_{total} (magenta bar in fig 5c). The values of I_H at 4 Hz are not much different from 1 Hz (fig 5d). However, I_{Ca} peaks at a much later phase (fig 5d right), which does not allow it to compensate for I_L + I_{Cm} at high voltages, thus resulting in a larger I_{total} (magenta bar in fig 5d). Note that at 1 Hz, the total current peaks at a cycle phase close to 0.5, thus implying that that the f_{res} and $f_{\phi=0}$ are very close or equal (fig 5c right). Although figure 5 shows the results for only one model in the optimal dataset, these results remain nearly identical for all models in the optimal dataset. The standard deviation of the currents measured, including the total current was never above 0.15 nA over all models. The inset in fig. 5c shows one standard deviation around the mean for the data shown in the right panel, calculated for 200 randomly selected models.

An important collective property of the models we found is that the two frequencies, f_{res} and $f_{\phi=0}$ coincide (fig. 6a-b). We analyzed the experimental data, and confirmed that the coincidence of MPR and phasonance frequencies also occurs in the biological system (fig. 6b inset). This is typically not the case for neuronal models (and for dynamical systems in general), not even for linear systems [18-20], with the exception of the harmonic oscillator. However, the fact that it occurs in this system, allows us to use the current vs. cycle phase (current-phase) diagrams to understand the dependence of f_{res} and $f_{\phi=0}$ on the model parameters (fig. 6c).

The current-phase diagrams are depicted as in fig 5b-d, as graphs of I_{total}, I_L and I_{Ca} as a function of the cycle phase for each given specific input frequency (fig. 6c). We do not show I_H and I_{Cm} in this plot, because at frequencies near f_{res} they do not change much with input frequency. Note that I_L is independent of the input frequency (five panels in fig. 6c) because it precisely tracks the input voltage.

In voltage clamp, $f_{\phi=0}$ = 1Hz is where I_{total} is at its minimum amplitude exactly at cycle phase 0.5, coinciding with the peak of the input voltage (fig. 6c, middle). The fact that I_L precisely tracks the input voltage imposes a constraint on the shapes of I_{Ca} and I_{total}. Therefore, by necessity, if the I_{Ca} trough occurs for a cycle phase below 0.5, the I_{total} peak must occur for a cycle phase above 0.5 (fig. 6-c, top two panels) and vice versa (fig. 6c, bottom two panels). This is shown by the slope of the line joining the peaks of I_{total} and I_{Ca} and, at f_{res} this line is approximately vertical (fig. 5c middle panel).

We use this tool to explain the dependence of the *Z*-profile on the time constants τ_m^{Ca} (fig. 7a) and τ_h^{Ca} (fig. 7b). The corresponding current-phase diagrams are presented in figs. 7c and 7d, respectively. In

each panel we present the current-phase diagrams for f at 1 Hz (=f_{res} when the parameter is at 100%; middle) and $f = f_{res}$ (sides) when f_{res} is different from 1Hz.

To understand the dependence of Z on changes in τ_m^{Ca} and τ_h^{Ca} we have to primarily explain the dependence of the two attributes Z_{max} and f_{res} on these parameters. While f_{res} has a similar monotonic dependence on τ_m^{Ca} and τ_h^{Ca} (as these parameters increase, f_{res} decreases), Z_{max} has the opposite dependence on τ_m^{Ca} and τ_h^{Ca}. The opposite dependence of Z_{max} on τ_m^{Ca} and τ_h^{Ca} is a straightforward consequence of the opposite feedback effects (positive for τ_m^{Ca} and negative for τ_h^{Ca}) that these parameters exert on I_{Ca}. An increase in τ_m^{Ca} (for fixed values of τ_h^{Ca}) results in a smaller I_{Ca} in response to a given voltage clamp input. Because I_{Ca} is smaller and negative, this leads to an increase in I_{total} and a decrease in Z at all frequencies. Similarly, an increase in τ_h^{Ca} (for fixed values of τ_m^{Ca}) results in a larger I_{Ca}, leading to a decrease in I_{total} and an increase in Z.

For a fixed value of the input frequency f (e.g. f = 1 Hz as in fig. 7), for Z_{max} to decrease as τ_m^{Ca} increases (fig. 7-a), the cycle phase of peak I_{Ca} is delayed thereby subtracting less from I_L on the depolarizing phase. This leads to I_{total} to phase advance relative to I_L (fig. 7-c) and causes f_{res} to decrease. Similarly, for Z_{max} to increase as τ_h^{Ca} increases (fig. 7-b), I_{Ca} has to peak later in the cycle thereby subtracting less from I_L on the depolarizing phase, which causes I_{total} to peak earlier in the cycle, which in turn causes the bar also to swing from the left to the right (fig. 7-d). Therefore, f_{res} decreases.

Parameter constraints and pairwise correlations

Previous studies have shown that stable network output can be produced by widely variable ion channel and synaptic parameters [37, 40]. Our biological data, similarly, showed that many of the Z- and ϕ-profile attributes, such as f_{res}, $\Lambda_{½}$ and $f_{\varphi=0}$ are relatively stable across different PD neurons whereas Q_Z shows the most variability (fig 3d). To determine whether the Z- and ϕ-profile attributes constrain ionic current parameters, we examined the variability of the model parameters in the optimal dataset. We found that some parameters were more constrained while others were widely variable, as measured by the coefficient of variation (CoV; fig 8a). Parameters showing large CoVs were $\bar{g}_{Ca}$, τ_m^h, $\bar{g}_h$, τ_h^{Ca}, and $V_{1/2}^{Ca_\infty^h}$; those showing small CoVs were $\bar{g}_L$ and the time constant of activation of I_H and I_{Ca} and half-

activation voltage of I_{Ca}: τ_m^{Ca}, $V_{1/2}^{Ca_\infty^m}$, $\bar{g}_L$ (in increasing order of CoV value). A small CoV value implies that the parameter is tightly constrained in order to produce the proper Z- and φ-profiles.

A number of studies have indicated that the large variability in ion channel parameters is counter-balanced by paired linear covariation of these parameters [36, 37, 41-43]. Considering the large variability, we identified parameter pairs that co-varied (fig 8b). For this, we carried out a permutation test for the Pearson's correlation coefficients, followed by a Student's t-test on the regression slopes, to identify significant correlations between pairs of parameters (see Methods). The strongest correlations were between the following parameters: $\bar{g}_L$ - $\bar{g}_H$ (r=-0.93), $\bar{g}_L$ - τ_m^{Ca} (R = 0.73), $\bar{g}_L$ - τ_h^{Ca} (R = 0.88), $\bar{g}_H$ - τ_m^H (R = 0.68), $\bar{g}_H$ - τ_h^{Ca} (R = -0.82), $\bar{g}_H$ - $V_{1/2}^{Ca_\infty^h}$ (R = 0.76), $\bar{g}_{Ca}$ - $V_{1/2}^{Ca_\infty^h}$ (R = -0.94), and τ_m^{Ca} - τ_h^{Ca} (R = -0.80) (correlations selected with $p < 0.01$; fig 8b).

In our experiments, $V_{1/2}^{H_\infty^m}$ was fixed at -70 mV, using data from experimental measurements in crab [44] (see Methods). However, we also repeated the MOEA with $V_{1/2}^{H_\infty^m}$ set to -96 mV, as reported in lobster experiments [45], and found that all correlations observed with the former value of $V_{1/2}^{H_\infty^m}$ remain intact, but simply with a much larger maximal conductance of I_H (fig. S1). In other words, shifting $V_{1/2}^{H_\infty^m}$ to the left simply results in larger $\bar{g}_H$ in the optimal models without qualitatively changing the other findings.

In particular, we found that the $\bar{g}_{Ca}$ - $V_{1/2}^{Ca_\infty^h}$ correlation appeared nonlinear, but there were strong and distinct linear correlations in the two regions $\bar{g}_{Ca}$ > 0.05 µS (low $\bar{g}_{Ca}$) and $\bar{g}_{Ca}$ < 0.05 µS (high $\bar{g}_{Ca}$; fig 8c). To ensure that our partitioning of the population into different levels of $\bar{g}_{Ca}$ was valid, we ran the MOEA two additional times, each time using only the mean values of $\bar{g}_L$, τ_m^H, $V_{1/2}^{Ca_\infty^m}$, and τ_m^{Ca} for either the low or the high $\bar{g}_{Ca}$ values. These optimal models consistently separated into two non-overlapping model parameters, consistent with the low and high $\bar{g}_{Ca}$ models in fig 8c.

We examined if the low and high $\bar{g}_{Ca}$ models separated or showed distinct correlations in the remaining parameters. The two groups produced non-overlapping subsets of model parameters in the $\bar{g}_{Ca}$ - $V_{1/2}^{Ca_\infty^h}$ graph. We calculated the Pearson's correlation coefficient for each pair of parameters in the low and high $\bar{g}_{Ca}$ groups and tested for significance as before (see Table 2). We found that only the high $\bar{g}_{Ca}$ group showed a significant τ_m^{Ca} - τ_h^{Ca} and $\bar{g}_H - \tau_h^{Ca}$ correlations (Table 2). Additionally, both low and high

263 $\bar{g}_{Ca}$ groups showed the following correlations: $V_{1/2}^{Ca_\infty^h} - \tau_h^{Ca}$, $\bar{g}_L$ - $\bar{g}_H$, $\bar{g}_{Ca}$ - $V_{1/2}^{Ca_\infty^h}$, and $\bar{g}_H - \tau_m^H$, $\bar{g}_{Ca} - \tau_h^{Ca}$.
264 Furthermore, when we ran the MOEA on models where $\bar{g}_H$ was set to 0, the only optimal models
265 obtained fell within a narrow range of the high $\bar{g}_{Ca}$ group (fig S2), which is consistent with the
266 distribution of high $\bar{g}_{Ca}$ models in the $\bar{g}_H - \bar{g}_{Ca}$ panel of figure 8d.

267

268 Decreasing the lower bound of voltage oscillations influences the measured f_{res}
269 and Z_{max}

270 The lower voltage range of the PD bursting oscillation is strongly influenced by the inhibitory synaptic input from
271 the lateral pyloric neuron (LP), and previous work has shown that f_{res} in the PD neuron is influenced by the
272 minimum of the voltage oscillation (V_{low}) [14]. In order to explore which subset of our optimal models faithfully
273 reproduce the influence of the minimum voltage range, we measured the Z-profile when V_{low} was changed from -
274 60 to -70 mV (fig 9a). Decreasing V_{low} significantly decreased f_{res} (by 0.24±0.8Hz), while there was no significant
275 difference in the mean Z_{max} (-0.15±0.81MΩ) (two-way RM-ANOVA; N = 8, $p < 0.001$; fig 9b, left panel).

276 To explore whether the shift in f_{res} as a function of V_{low} could be captured by either low or high $\bar{g}_{Ca}$ models, we
277 measured the shift in f_{res} and Z_{max}, when V_{low} was changed from -60mV to -70mV. We found that f_{res} decreased by
278 0.24±0.03 Hz and Z_{max} increased by 5.2±0.6 MΩ for high $\bar{g}_{Ca}$ models, whereas f_{res} decreased by 0.07±0.02Hz and
279 Z_{max} decreased by 2.6±0.2MΩ for low $\bar{g}_{Ca}$ models (fig 9b, right panel). Therefore, neither model group reproduced
280 the experimental changes in the Z-profile, specifically, a decrease in f_{res} and no change in Z_{max}.

281 We consequently filtered the full optimal dataset (black dots fig 9c) to find a subset of models that reproduced the
282 change in f_{res} and Z_{max} (to within 5% of the representative experimental Z(f) shown in fig 9a) when V_{low} was
283 decreased to -70mV. Of the ~9000 models in the population, we found ~1000 models that produced the desired
284 change. Interestingly, the resulting models showed a trade-off in values for $\bar{g}_{Ca}$ and $V_{1/2}^{Ca_\infty^h}$ parameters that showed
285 little overlap with the low and high $\bar{g}_{Ca}$ model groups (fig 9c).

286 To understand why this particular group (which we will term intermediate $\bar{g}_{Ca}$) produced small changes in Z_{max}
287 when V_{low} was decreased, we plotted the current-voltage relationships for I_{Ca}, I_H, I_{Ca}+I_H and I_{total} for V_{low} = -60 and -
288 70 mV, measured at f=1Hz (f_{res} at V_{low} = -60mV) and compared these models with the low and high $\bar{g}_{Ca}$ models. For
289 V_{low} =-60mV, the ionic currents behaved similarly for all model groups and I_{total} was maximal at -30mV (magenta
290 curve in fig 9d1-3), indicating the similarity of all models in the optimal dataset. However, when V_{low} was at -70mV

revealed differences in peak I_{Ca}, without affecting the peak amplitude of I_H across the different $\bar{g}_{Ca}$ groups (fig 9e1-3). The differences in peak I_{Ca} accounted for most of the changes in I_{total} across the different $\bar{g}_{Ca}$ groups. The Z_{max} values for intermediate $\bar{g}_{Ca}$ models reproduced the small shift seen in experiments because I_{Ca} were at the correct level at high voltages (-30 mV) when V_{low} was at -70mV (fig 9e3). The other two groups did not produce appropriate Z_{max} for V_{low} = -70mV because either I_{Ca} was too small (and hence I_{total} too large), resulting in a smaller Z_{max} (fig 9e1) or vice versa (fig 9e2). It was also clear that the more negative voltages allowed for an increase in I_H levels and therefore larger contribution to the total current. With V_{low} at -70mV, not only was there a larger peak amplitude of I_H at the lower voltages, but the current at positive voltages also increased because of the very slow deactivation rate. Consequently, I_H did not fully turn off when I_{Ca} peaked, so that it also contributes to shaping the upper envelope of the total current. I_H kinetics were different across the groups (fig 9e1-e3). Taken together with the fact that when I_H was removed produced only parameter values with very high $\bar{g}_{Ca}$ and very low $V_{1/2}^{Ca_\infty^h}$ (fig S1), these data suggest that I_H could extend the range of I_{Ca} parameters over which MPR through compensation for variable levels of I_H.

The I_{Ca} in low $\bar{g}_{Ca}$ models was too small when V_{low} was -70 mV, because the low conductance did not allow for a significant contribution from the additional de-inactivation (considering the higher $V_{1/2}^{Ca_\infty^h}$ in this group) and therefore the peak current did not increase enough. Consequently, the contribution of I_H at low voltages was greater than that of I_{Ca} at higher voltages (fig 9e2). Conversely, in the high $\bar{g}_{Ca}$ group, $V_{1/2}^{Ca_\infty^h}$ was more negative and so many more channels were available for de-inactivation and the contribution of I_{Ca} at higher voltages was much larger than that of I_H at low voltages (fig 9e3). These findings suggest that the balance between these two currents, that shape the lower and upper envelope of the total current response to voltage inputs, is necessary to produce the appropriate shift in f_{res} without influencing Z_{max} significantly.

The intermediate $\bar{g}_{Ca}$ models were strongly correlated in $\bar{g}_{Ca}$ - $V_{1/2}^{Ca_\infty^h}$ (R^2 = 0.89; p < 0.001 fig 9f1, and had a stronger correlation in the τ_m^{Ca} - τ_h^{Ca} parameters compared to all models (R^2 = 0.65; p < 0.001; fig 9g). Limiting the optimal models to the intermediate $\bar{g}_{Ca}$ group also revealed a correlation in the $\bar{g}_{Ca}$ - $\bar{g}_H$ parameters (R^2 = 0.79; p < 0.001; fig 9h). This new correlation may be produced by the balance of the amplitudes of I_H and I_{Ca} at the lower and higher voltages, respectively.

f_{res} and Q_z are maintained by distinct pairwise correlations

To determine if any of the MPR attributes were sensitive to the correlations, we ran a 2D sensitivity analysis on a random subset of 50 models. We tested for significant difference in sensitivity across low, intermediate and high levels of $\bar{g}_{Ca}$. In particular, we tested for significant sensitivity of f_{res} *and* Q_Z when parameters were co-varied in directions parallel (L) or perpendicular ($L^{\perp}$) to their respective population correlation lines.

We first examined whether f_{res} and Q_Z were sensitive to $\tau_m^{Ca} - \tau_h^{Ca}$ for both high (fig 10a1), low (fig 10a2), and intermediate $\bar{g}_{Ca}$ (fig 10a3) when parameters were moved along L and $L^{\perp}$ (blue and green line; fig 10a1-a3). For high and intermediate $\bar{g}_{Ca}$ models, f_{res} sensitivities in the L group were negative and not significantly different (3-way RM ANOVA; N=50, $p > 0.05$), but both groups were significantly different from the low $\bar{g}_{Ca}$ group (3-way RM ANOVA; N=50, $p < 0.001$), which had a positive sensitivity (fig 10b). This result indicates that the correlation did a better job at maintaining the value of f_{res} when the value of $\bar{g}_{Ca}$ is intermediate or high. For all $\bar{g}_{Ca}$ groups, we found that there was a significant interaction between the Z attribute and direction (2-way RM ANOVA; $F(1, 49) = 853.52$, $p < 0.001$). When carrying out a pairwise comparison for each direction within an attribute, we found a significant difference in sensitivity between L and $L^{\perp}$ for f_{res} ($t(93.57)=28.251$, $p<0.001$). Similarly, for all $\bar{g}_{Ca}$ groups, significant difference in sensitivity between L and $L^{\perp}$ for Q_Z ($t(93.57)=-8.294$, $p<0.001$). Because the difference between L and $L^{\perp}$ for Q_Z was negative, these results suggest that the $\tau_m^{Ca} - \tau_h^{Ca}$ correlation determines f_{res} and not Q_Z (fig 10b).

We next examined whether f_{res} and Q_Z were sensitive to the $\bar{g}_{Ca} - V_{1/2}^{Ca_\infty^h}$ correlation for the three model groups (fig 11a1-3). For all $\bar{g}_{Ca}$ groups, we found that there was a significant interaction between the Z attribute and direction (2-way RM ANOVA; $F(1, 49) = 1262.73.2$, $p < 0.001$). When carrying out a pairwise comparison for each direction within an attribute, we found a significant difference in sensitivity between L and $L^{\perp}$ for f_{res} ($t(95.18)=10.10$, $p<0.001$). Similarly, for all $\bar{g}_{Ca}$ groups, we found a significant difference in sensitivity between L and $L^{\perp}$ for Q_Z ($t(95.18)=-35.62$, $p<0.001$). Therefore, these results suggest that the $\bar{g}_{Ca} - V_{1/2}^{Ca_\infty^h}$ correlation determines Q_Z and not f_{res} (fig 11b).

Finally, we tested the sensitivity of f_{res} and Q_Z to the $\bar{g}_{Ca} - \bar{g}_H$ correlation in the intermediate $\bar{g}_{Ca}$ group (fig 12a). We found that there was a significant interaction between the Z attribute and direction (2-way RM ANOVA; $F(1, 11.12) = 2236.2$, $p < 0.001$). When carrying out pairwise comparisons between

directions for each attribute, we found there was a significant difference in f_{res} sensitivity between L and $L^{\perp}$ ($t(93.93) = 2.65$, $p = 0.0095$; fig 12). Although the sensitivity of Q_Z was not 0 for L , the difference in sensitivity values between L and $L^{\perp}$ was also significantly different ($t(93.93) = 62.157$, $p < 0.0001$; fig 12b). These results suggest that, when V_{low} is at -70 mV, for this subset of models to shift f_{res} with only small shifts in Z_{max}, $\bar{g}_H$ and $\bar{g}_{Ca}$ values must be balanced. It may be possible that the Q_Z sensitivity is not closer to zero along L because $V_{1/2}^{Ca_\infty^h}$, which is also negatively correlated with $\bar{g}_{Ca}$, should decrease too to compensate for changes in Q_Z.

Discussion

Many neuron types exhibit membrane potential resonance (MPR) in response to oscillatory inputs. Several studies have shown that the resonant frequency of individual neurons is correlated with the frequency of the network in which they are embedded [2, 6, 12, 14, 22, 46]. Moreover, networks of resonant neurons have been proposed to generate more robust network oscillations than neurons with low-pass filter properties [27, 28]. In several cases, the underlying nonlinearities and time scales that shape the Z-profile also shape specific properties of the spiking activity patterns, thus leading to a link between the subthreshold and suprathreshold voltage responses [25, 47].

Previous work in the crustacean stomatogastric pyloric network has shown that the resonance frequency of the pyloric pacemaker PD neurons is correlated with the pyloric network frequency and is sensitive to blockers of both I_H and I_{Ca} [12-14]. However, it was not clear how these voltage-gated ionic currents and the passive properties could interact to generate MPR in the PD neurons. Previous modeling work showed that these currents participate in the generation of resonance in CA1 pyramidal neurons [16, 17]. However, due to the differences in I_{Ca} time constants, the interaction between its activating and inactivating gating variables did not produce phasonance in CA1 pyramidal neurons, while it does in PD neurons. On a more general level, it is not well understood how the nonlinear properties of ionic currents affect their interplay. Previous studies have shown such interactions may lead to unexpected results, which are not captured by the corresponding linearizations [16-19]. This complexity is expected to increase when two currents with resonant components are involved [16, 48]. We therefore set out to investigate the biophysical mechanism underlying such interactions by using a combined experimental and computational approach and the biological PD neuron as a case study. The two PD neurons are electrically coupled to the pacemaker anterior burster neuron in the pyloric network and their MPR directly influences the network frequency through this electrical coupling [22]. Consequently, our findings have a direct bearing on how the pyloric network frequency is controlled.

Many studies of biophysical models have explored the parameter space using a brute-force technique, by sampling the parameters on a grid [40, 49]. Although this technique provides a rather exhaustive sampling of the parameter space, using a fine grid on a large number of free parameters could lead to combinatorial explosion and result in a prohibitive number of simulations. On the other hand, a sparse sampling may miss “good” solutions. A multi-objective evolutionary algorithm (MOEA) can generate multiple trade-off solutions in a single run and can handle large parameter spaces very well. In contrast

to a brute-force approach, the MOEA can potentially cover a much larger range with possibly hundreds of values [38]. One disadvantage of the MOEA is that, as the number of objectives increases, the search may miss a large portion of the parameter space. This occurs because randomly generated members often tend to be just as good as others, which means that the MOEA would run out of room to introduce new solutions in a given generation. To try to overcome this problem, we carefully chose the parameters of the MOEA such as population size, mutation and crossover distribution indices (100, 20 and 20, respectively) and ensured that the sampled population covered the parameter space evenly. Additionally, we ran the MOEA multiple times, each time collecting all the good parameter sets until one has exhausted all regions of the parameter space where good models exist.

In previous work, we and other authors have examined how the additive interaction of ionic currents with resonant and amplifying gating variables shape the Z and ϕ profiles at both the linear and nonlinear levels of description [6, 15, 18, 20, 32, 33, 50]. However, the role of inactivating currents in the generation of MPR is not so clear. Authors have established that I_{Ca} can generate MPR in the absence of additional ionic currents [21], that the activation variable diminishes the propensity for MPR and the interaction with I_H enhances the dynamic range of parameters producing I_{Ca}-mediated resonance [16]. Even so, to date, only a descriptive explanation of how the ionic current parameters affect certain attributes of MPR has been provided, but no study has provided a mechanistic understanding in terms of the parameters of I_{Ca} that go beyond numerical simulations.

Similar to [16], the model we used in this paper involves the interaction between resonant and amplifying components. Specifically, this model includes a calcium current with both activation (amplifying) and inactivation (resonant) gating variables, and an H-current with a single activation (resonant) gate. Since I_H and I_{Ca} shape the lower and upper envelopes of the voltage response to current inputs, respectively [12], given the appropriate voltage-dependence and kinetics of the currents both could play equal roles at different voltage ranges. In fact, either I_{Ca} inactivation or I_H is capable of producing MPR [2, 21]. In CA1 pyramidal neurons, the differences in Z profiles are due to the passive properties and the kinetics of I_H [4]. It is possible that the kinetic parameters of I_H and I_{Ca} are tuned so that they contribute nearly equally to shaping the envelopes of the voltage-clamp current.

By tracking the current response to sinusoidal voltage inputs at various frequencies, we found that the f_{res} and $f_{\phi=0}$ are driven by the peak phase of $I_{Ca,}$ and that f_{res} and $f_{\phi=0}$ are nearly equal because of the phase matching of I_{Ca} with I_L. This is not always the case for neuronal models, and dynamical systems in

general, not even for linear models, except for the harmonic oscillator [18-20]. In fact, as we mentioned above, this is not the case for the I_{Ca} model used in [16], although our results on the I_{Ca} inactivation time constant are consistent with that study. In these models phase advance for low input frequencies required the presence of I_H. The underlying mechanisms are still under investigation and are beyond the scope of this paper. However, the fact that it occurs was crucial to develop a method to investigate the dependence of the resonant properties, particularly the dependence of the f_{res} on the I_{Ca} time constants, using phase information. To date, no other analytical method is available to understand the mechanisms underlying this type of phenomenon in voltage clamp. The tools we developed are applicable to other neuron types for which f_{res} is equal to or has a functional relationship with $f_{\varphi=0}$. However, the conditions under which such a functional relationship exists still needs to be investigated.

Linear correlations between biophysical parameters of the same or different currents have been reported [37] and may be important in preserving the activity of the model neuron and its subthreshold impedance profile attributes [41]. Previous studies examined combinations of parameters in populations of multi-compartment conductance-based models fit to electrophysiological data [16, 51] and found only weak pairwise correlations suggesting that the correlations do not arise from electrophysiological constraints. In contrast, constraining the parameters of the ionic currents found to be essential for MPR in PD neuron by MPR attributes, we observed strong correlations underlying parameters when the Z and ϕ were constrained by the experimental data. We found that constraining the model parameters by f_{res} produced a correlation between the values of time constants of I_{Ca} among the population of ~9000 optimal parameter sets. Furthermore, running a 2D sensitivity analysis confirmed that the time constants were constrained so that the effect of making inactivation slower was compensated for by making activation faster to maintain f_{res} constant.

The optimal model parameter sets showed a nonlinear co-variation relationship between the $\bar{g}_{Ca}$ and half-inactivation voltage of I_{Ca}. However, the models could be divided into two groups, low and high $\bar{g}_{Ca}$ in each of which this co-variation was close to linear. Interestingly, although I_{Ca} alone was the primary current underlying MPR, in the absence of I_H (with $\bar{g}_H = 0$) the models were restricted to the high $\bar{g}_{Ca}$ group. A 2D sensitivity analysis showed that co-varying parameters in each groups along their respective correlation lines preserved Q_Z without affecting f_{res}, indicating that each group requires a distinct changes in one parameter to compensate for effects of changes in the other. Local sensitivity analysis showed that changes in $V_{1/2}^{Ca_\infty^h}$ had opposite effects on f_{res} between high and low $\bar{g}_{Ca}$ groups.

Increasing $V_{1/2}^{Ca_\infty^h}$ decreased f_{res} in high $\bar{g}_{Ca}$ models but increased it in low $\bar{g}_{Ca}$ models. A previous modeling study has found that changes in $V_{1/2}^{Ca_\infty^h}$ greatly influenced the amplitude of MPR with little effect on post-inhibitory rebound in thalamic neurons [21]. It would be interesting to verify whether the mechanisms that generate MPR overlap with those that contribute to post-inhibitory rebound properties.

Previous work in our lab has shown that the voltage range of oscillations significantly affects f_{res} [13]. Here we show that decreasing, V_{low}, the lower bound of the oscillation voltage of the PD neuron, from -60 to -70 mV, significantly shifted f_{res} to smaller values without affecting Z_{max}. Within our optimal model parameter sets, we obtained a set of ~1000 models in the intermediate $\bar{g}_{Ca}$ range that produced a similar shift in f_{res} but no change in Z_{max}. Because V_{low} greatly affects both I_{Ca} inactivation and I_H activation, this indicated a potential interaction between these two currents. In fact, we found that because I_H and I_{Ca} are activated preferentially in different voltage ranges, their amplitudes needed to be balanced to keep Z_{max} unchanged when V_{low} was decreased. If the ratio of I_H to I_{Ca} amplitudes is incorrect, then Z will amplify (for high $\bar{g}_{Ca}$ models) or attenuate (for low $\bar{g}_{Ca}$ models). The intermediate $\bar{g}_{Ca}$ models also showed a stronger τ_m^{Ca} - τ_h^{Ca} correlation, which may be important in matching the phase of I_{Ca} with that of I_L. This group also showed a strong $\bar{g}_H - \bar{g}_{Ca}$ correlation, which may provide a mechanism for controlling the changes in I_H amplitude at more negative voltage with similar changes in I_{Ca} amplitude at more positive voltages.

In contrast to the findings of Rathour and Narayanan [16], in our optimal models the I_H amplitude was not different across the groups with different I_{Ca} properties. However, since I_{Ca} and I_H are differentially modulated [45, 52], their functional role may overlap when their voltage thresholds and time constants are shifted by neuromodulation. Therefore, we expect that under certain neuromodulatory contexts, I_H may play more of an active role in the generation of MPR. A similar effect of two ionic currents on resonance has been observed in the hippocampal pyramidal cells that participate in the theta rhythm, in which two currents, the slow potassium M-current and I_H, were found to operate at the depolarized and hyperpolarized membrane potentials respectively to generate theta-resonance [2].

In general, variability of ionic current expression in any specific neuron type should lead to great variability in network output. Yet, network output in general, and specifically the output of the crustacean pyloric network is remarkably stable across animals [30, 53, 54]. Our results suggest that in

474 oscillatory networks the interaction among ionic currents in an individual neuron may be tuned in a way
475 that the variability of the output is reduced in response to oscillatory inputs. Although our
476 computational study may provide some insight into how such stability is achieved, it also indicates a
477 need for additional mathematical analysis to elucidate the underlying mechanisms.

478

479 Methods

480 Electrophysiology

481 The stomatogastric nervous system of adult male crabs *(Cancer borealis)* was dissected using standard
482 protocols as in previous studies [14]. After dissection, the entire nervous system including the
483 commissural ganglia, the esophageal ganglion, the stomatogastric ganglion (STG) and the nerves
484 connecting these ganglia, and motor nerves were pinned down in a 100mm Petri dish coated with clear
485 silicone gel, Sylgard 186 (Dow Corning). The STG was desheathed to expose the PD neurons for
486 impalement. During the experiment, the dish was perfused with fresh crab saline maintained at 10-
487 13ºC. After impalement with sharp electrodes, the PD neuron was identified by matching intracellular
488 voltage activity with extracellular action potentials on the motor nerves. After identifying the PD neuron
489 with the first electrode, a second electrode was used to impale the same neuron in preparation for two-
490 electrode voltage clamp. Voltage clamp experiments were done in the presence of 10^{-7} M tetrodotoxin
491 (TTX; Biotium) superfusion to remove the neuromodulatory inputs from central projection neurons
492 (decentralization) and to stop spiking activity [13, 14].

493 Intracellular electrodes were prepared by using the Flaming-Brown micropipette puller (P97; Sutter
494 Instruments) and filled with 0.6M K_2SO_4 and 0.02M KCl. For the microelectrode used for current
495 injection and voltage recording, the resistance was, respectively, 10-15MΩ and 25-35MΩ. Extracellular
496 recording from the motor nerves was carried out using a differential AC amplifier model 1700 (A-M
497 Systems) and intracellular recordings were done with an Axoclamp 2B amplifier (Molecular Devices).

498 Measuring the Z-profile

499 During their ongoing activity, the PD neurons produce bursting oscillations with a frequency of ~1 Hz
500 and slow-wave activity in the range of -60 to -30 mV. Activity in the PD neuron is abolished by

501 decentralization. The decentralized PD neuron shows MPR in response to ZAP current injection when
502 the current drives the PD membrane voltage to oscillate between -60mV and -30mV, which is similar to
503 the slow-wave oscillation amplitude during ongoing activity [12]. The MPR profiles are not significantly
504 different when measured in current clamp and voltage clamp [14]. Since the MPR depends on the
505 dynamics of voltage-gated ionic currents, it will also depend on the range and shape of the voltage
506 oscillation. Therefore, to examine how $Z(f)$ in a given voltage range constrains the properties of voltage-
507 gated currents and how factors that affect the voltage range change MPR, we measured $Z(f)$ in voltage
508 clamp [10].

509 To measure the Z-profile, the PD neuron was voltage clamped with a sweeping-frequency sinusoidal
510 impedance amplitude profile (ZAP) function [55] and the injected current was measured [14]. To
511 increase the sampling duration of lower frequencies as compared to the larger ones, a logarithmic ZAP
512 function was used:

513 $$ZAP(\mathrm{t}) = v_0 + v_1 \sin(2\pi F(t));\ F(t) = f_{lo} t \left(\frac{f_{hi}}{f_{lo}} \right)^{t/T}.$$

514 The amplitude of the ZAP function was adjusted to range between -60 and -30 mV (v_0=-45 mV, v_1=15
515 mV) and the waveform ranged through frequencies of f_{lo}=0.1 to f_{hi}=4 Hz over a total duration T=100 s.
516 Each ZAP waveform was preceded by three cycles of sinusoidal input at f_{lo} which smoothly transitioned
517 into the ZAP waveform. The total waveform duration was therefore 130 s.

518 Impedance is a complex number consisting of amplitude and phase. To measure impedance amplitude,
519 we calculated the ratio of the voltage and current amplitudes as a function of frequency and henceforth
520 impedance amplitude will be referred to as $Z(f)$. To measure φ_Z(f), we measured the time difference
521 between the peaks of the voltage clamp ZAP and the measured clamp current. One can also measure
522 $Z(f)$ by taking the ratio of the Fourier transforms of voltage and current. However, spectral leakage,
523 caused by taking the FFT of the ZAP function and the nonlinear response, often resulted in a low signal-
524 to-noise ratio and therefore in inaccurate estimates of impedance. Such cases would lead to less
525 accurate polynomial fits compared to the cycle-to-cycle method described above and we therefore
526 limited our analysis to the cycle-to-cycle method.

527 Because the average Z-profile may not be a realistic representation of a biological neuron, we used the
528 attributes of Z and ϕ measurements from a single PD neuron as our target. We characterized attributes

of Z into five objective functions used for fitting by specifying five points of the profile (fig 1a). These five points were:

- (f_0, Z_0), where $Z_0 = Z(f_0)$ and f_0 = 0.1 Hz,
- (f_{res}, Z_{max}), thereby capturing $Qz = Z_{max} - Z_0$,
- (f_1, $Z(f_1)$) where f_1 = 4 Hz,
- The two frequencies at which $Z = Z_0 + Q_Z / 2$. Pinning the profile to these points captures the frequency bandwidth $\Lambda_{½}$ which is the frequency range for which $f > Z_0 + Q_Z / 2$ (fig 1a).

We also constructed five objective functions to capture the attributes of $\varphi(f)$ at five points (fig 1b):

- (f_0, $\varphi(f_0)$),
- ($f_{\varphi=0}$, 0), where $f_{\varphi=0}$, is the phasonant frequency
- ($f_{\varphi max}$, φ_{max}) where φ_{max} is the maximum phase advance,
- ($f_{\varphi min}$, φ_{min}) where φ_{min} is the maximum phase delay,
- (2 Hz, $\varphi_{f=2}$) capturing the phase at 2Hz.

Single-compartment model

We used a single-compartment biophysical conductance-based model containing only those currents implicated in shaping Z and φ [12]. We performed simulations in voltage clamp and measured the current as:

$$I_{clamp} = I_{Cm} + I_L + I_{Ca} + I_H$$

where I_{Cm} is the capacitive current ($C\frac{dV}{dt}$ in nA), C_m is set to 1 nF and I_L is the voltage-independent leak current in nA. The voltage-dependent currents I_{curr} (I_{Ca} or I_H) in nA are given by

$$I_{curr} = \bar{g}_{curr} m_{curr}^p h_{curr}^q (V - E_{curr})$$

where V is the ZAP voltage input (see below), m_{curr} is the activation gating variable, h_{curr} is the inactivation gating variable, $\bar{g}_{curr}$ is the maximal conductance in µS, E_{curr} is the reversal potential in mV,

and p and q are non-negative integers. For I_{Ca}, $p = 3$, $q = 1$ and, for I_H, $p = 1$ and $q = 0$. The generic equation that governs the dynamics of the gating variables is:

$$\frac{dx}{dt} = \frac{1}{\tau_x}(x_\infty(V) - x)$$

where $x = m_{curr}$ or h_{curr}, and

$$x_\infty(V) = 1/\left[1 + \exp\left((V - V_x)/k_x\right)\right]$$

The sign of the slope factor (k_x) determines whether the sigmoid is an increasing (negative) or decreasing (positive) function of V, and V_x is the midpoint of the sigmoid.

A total of 8 free model parameters were defined (Table 1), which were optimized in light of the objective functions introduced above, to yield a good fit to the Z-profile attributes as described below. The slope factors k_x of the sigmoid functions $m_\infty^{Ca}(V)$, $h_\infty^{Ca}(V)$, and $m_\infty^{h}(V)$ were fixed at -8 mV, 6 mV, and -7 mV, respectively. $V_{1/2}^{H_\infty^m}$ was fixed at -70 mV, using data from experimental measurements in crab [44]. The voltage-dependent time constant for I_H was also taken from [44] to be

$$\tau_m^H / \left[1 + \exp\left((V + 110)/-13\right)\right]$$

where the range of τ_m^H is given in Table 1.

Fitting models to experimental Data

Computational neuroscience optimization problems have used a number of methods, such as the "brute-force" exploration of the parameter space [51] and genetic algorithms [56]. However, the brute-force method is computationally prohibitive for an 8-dimensional model parameter space, which would require potentially very fine sampling to find optimal models. [57]. We used an MOEA (evolutionary optimization) to identify optimal sets of model parameters constrained by experimental Z and φ attributes. MOEAs are computationally efficient at handling high-dimensional parameter spaces and other studies have used them to search for parameters constrained by other types of electrophysiological activity [57]

Evolutionary optimization finds solutions by minimizing a set of functions called objective functions, or simply objectives, subject to certain constraints. In our problem, each objective represents the Euclidean distance between the target and the model attributes of Z and φ. When optimizing multiple (potentially conflicting) objectives, MOEA will find a set of solutions that constitute trade-offs in objective scores. For instance, an optimal parameter set may include solutions that are optimal in f_{res} but not in Q_z or vice versa and a range of solutions in between that result from the trade-offs in both objectives. In this paper, we used the non-dominated sorting genetic algorithm II (NSGA-II) [38, 58] to find optimal solutions, which utilizes concepts of non-dominance and elitism, shown to be critical in solving multi-objective optimization problems [58]. Solution x_1 is said to dominate solution x_2 if it is closer to the target $Z(f)$ and $\varphi(f)$ profiles in at least one attribute (e.g., f_{res}) and is no worse in any other attributes (e.g., Q_Z, Z_0, etc.).

NSGA-II begins with a population of 100 parameter combinations created at random within pre-determined lower and upper limits (Table 1). The objective values for each parameter combination are calculated and ordered according to dominance. First, the highest rank is assigned to all of the non-dominated, trade-off solutions. From the remaining set of parameters, NSGA-II selects the second set of trade-off solutions. This process continues until there are no more parameter combinations to rank. Genetic operators such as binary tournament selection, crossover, and mutation form a child population. A combination of the parent and child parameter sets form the population used in the next generation of NSGA-II [38, 58]. NSGA-II favors those parameter combinations—among solutions non-dominating with respect to one another—that come from less crowded parts of the parameter search space (i.e., with fewer similar, in the sense of fitness function values, solutions), thus increasing the diversity of the population. The crowding distance metric is used to promote large spread in the solution space [38].

We ran NSGA-II multiple times (3-5 times, until the mean values of the distributions of optimal parameters was stable) each time for 200 generations with a population size of 100, and pooled the solutions at the end of each run to form a combined population of ~9000 parameter combinations. The algorithm stopped when no additional distinct parameter combinations were found. The Z and φ values associated with the optimal parameter sets match the target features (objectives) defining Z and φ to within 5% accuracy.

To test whether two parameters were significantly correlated in the population of 9000 PD models, we calculated the Pearson's correlation coefficients for each pair of parameters and used a permutation test to determine the number of times the calculated correlation coefficient (using a random subset of 20 models). The p-value was given as the fraction of R-values for the permuted vectors greater than the R-value for the original data [51]. We also used a t-test to determine whether the calculated slope of the

608 linear fit differed significantly from zero, which gave us identical results. We repeated both procedures
609 2000 times, each time with a random subset of 20 models and calculated the percentage of times we
610 obtained a p-value < 0.01.

611

612 **Sensitivity Analysis**

613 We assessed how the values of f_{res} and Q_Z depend on changes in parameter values by performing a
614 sensitivity analysis as in [59]. We split the model parameters into two categories: additive, for the
615 voltage-midpoints of activation and inactivation functions, and multiplicative, for the maximal
616 conductances and time constants. We changed the parameters one at a time and fit the relative change
617 in the resonance attributes as a linear function of the relative parameter change. We changed the
618 multiplicative parameters on a logarithmic scale to characterize parameters with both low and high
619 sensitivity.

620 Multiplicative parameters were varied as $p_{n+1} = \exp(\pm\Delta p_n)\, p_0$ with $\Delta p_n = 0.001*1.15^n$ and the sign
621 indicating whether the parameter was increased or decreased. To ensure approximate linearity, we
622 added points to the fit until the R^2 value fell below 0.98. The sensitivity was defined as the slope of this
623 linear fit (fig 2). For example, if a resonance attribute has a sensitivity of 1 to a parameter, then a 2-fold
624 change in the parameter results in a 2-fold change in the attribute. We changed additive parameters by
625 ±0.5 mV.

626 We assessed the sensitivity of f_{res} and Q_z to parameter pairs (p_1 and p_2) that were correlated. We first fit
627 a line through the correlated values in the p_1-p_2 space. We then shifted this line to pass through a subset
628 of 50 random points in p_1-p_2 space, resulting in a family of parallel lines, L . For each point, we also
629 produced a line perpendicular to a line $L^{\perp}$. For each model, we performed a sensitivity analysis as before
630 but used the linear fit equation L or $L^{\perp}$ to calculate value of p_2. We fit the relative change in the Z(f)
631 attribute as a linear function of the correlated change in p_1 and p_2. We used the slope of the linear fit to
632 represent the sensitivity. We used a 2-and 3-way repeated measures ANOVA and the lsmeans function
633 in R to perform pairwise comparisons of means in testing for significant differences between each group
634 of g_{Ca}, each direction, L and $L^{\perp}$, and between each Z attribute, f_{res} and Q_Z.

For each model, we solved a system of three differential equations for m_H, m_{Ca} and h_{Ca} (voltage was clamped). All simulations were performed using the modified Euler method [60] with a time step of 0.2 ms. The simulation code, impedance calculations, and MOEA were written in C++. MATLAB (The MathWorks) and R were used to perform statistical analyses.

References

1. Hutcheon B, Yarom Y. Resonance, oscillation and the intrinsic frequency preferences of neurons. Trends Neurosci. 2000;23(5):216-22. PubMed PMID: 10782127.
2. Hu H, Vervaeke K, Storm JF. Two forms of electrical resonance at theta frequencies, generated by M-current, h-current and persistent Na+ current in rat hippocampal pyramidal cells. J Physiol. 2002;545(Pt 3):783-805. PubMed PMID: 12482886; PubMed Central PMCID: PMCPMC2290731.
3. Pike FG, Goddard RS, Suckling JM, Ganter P, Kasthuri N, Paulsen O. Distinct frequency preferences of different types of rat hippocampal neurones in response to oscillatory input currents. J Physiol. 2000;529 Pt 1:205-13. PubMed PMID: 11080262; PubMed Central PMCID: PMC2270176.
4. Zemankovics R, Kali S, Paulsen O, Freund TF, Hajos N. Differences in subthreshold resonance of hippocampal pyramidal cells and interneurons: the role of h-current and passive membrane characteristics. J Physiol. 2010;588(Pt 12):2109-32. doi: 10.1113/jphysiol.2009.185975. PubMed PMID: 20421280; PubMed Central PMCID: PMCPMC2905616.
5. Erchova I, Kreck G, Heinemann U, Herz AV. Dynamics of rat entorhinal cortex layer II and III cells: characteristics of membrane potential resonance at rest predict oscillation properties near threshold. J Physiol. 2004;560(Pt 1):89-110. doi: 10.1113/jphysiol.2004.069930. PubMed PMID: 15272028; PubMed Central PMCID: PMC1665205.
6. Schreiber S, Erchova I, Heinemann U, Herz AV. Subthreshold resonance explains the frequency-dependent integration of periodic as well as random stimuli in the entorhinal cortex. J Neurophysiol. 2004;92(1):408-15. doi: 10.1152/jn.01116.2003. PubMed PMID: 15014100.
7. Lampl I, Yarom Y. Subthreshold oscillations of the membrane potential: a functional synchronizing and timing device. J Neurophysiol. 1993;70(5):2181-6. PubMed PMID: 8294979.
8. Lampl I, Yarom Y. Subthreshold oscillations and resonant behavior: two manifestations of the same mechanism. Neuroscience. 1997;78(2):325-41. PubMed PMID: 9145790.
9. Puil E, Meiri H, Yarom Y. Resonant behavior and frequency preferences of thalamic neurons. J Neurophysiol. 1994;71(2):575-82. PubMed PMID: 8176426.
10. Beatty JA, Song SC, Wilson CJ. Cell-type-specific resonances shape the responses of striatal neurons to synaptic input. J Neurophysiol. 2015;113(3):688-700. doi: 10.1152/jn.00827.2014. PubMed PMID: 25411465; PubMed Central PMCID: PMCPMC4312866.
11. Song SC, Beatty JA, Wilson CJ. The Ionic Mechanism of Membrane Potential Oscillations and Membrane Resonance in Striatal LTS Interneurons. J Neurophysiol. 2016:jn 00511 2016. doi: 10.1152/jn.00511.2016. PubMed PMID: 27440246.
12. Tohidi V, Nadim F. Membrane resonance in bursting pacemaker neurons of an oscillatory network is correlated with network frequency. J Neurosci. 2009;29(20):6427-35. doi: 10.1523/JNEUROSCI.0545-09.2009. PubMed PMID: 19458214; PubMed Central PMCID: PMC2716082.
13. Tseng HA, Martinez D, Nadim F. The frequency preference of neurons and synapses in a recurrent oscillatory network. J Neurosci. 2014;34(38):12933-45. doi: 10.1523/JNEUROSCI.2462-14.2014. PubMed PMID: 25232127; PubMed Central PMCID: PMC4166170.
14. Tseng HA, Nadim F. The membrane potential waveform of bursting pacemaker neurons is a predictor of their preferred frequency and the network cycle frequency. J Neurosci. 2010;30(32):10809-19. doi: 10.1523/JNEUROSCI.1818-10.2010. PubMed PMID: 20702710; PubMed Central PMCID: PMC2944831.
15. Richardson MJ, Brunel N, Hakim V. From subthreshold to firing-rate resonance. J Neurophysiol. 2003;89(5):2538-54. doi: 10.1152/jn.00955.2002. PubMed PMID: 12611957.
16. Rathour RK, Narayanan R. Inactivating ion channels augment robustness of subthreshold intrinsic response dynamics to parametric variability in hippocampal model neurons. J Physiol.

2012;590(22):5629-52. doi: 10.1113/jphysiol.2012.239418. PubMed PMID: 22930270; PubMed Central PMCID: PMCPMC3528982.

17. Rathour RK, Narayanan R. Homeostasis of functional maps in active dendrites emerges in the absence of individual channelostasis. Proceedings of the National Academy of Sciences of the United States of America. 2014;111(17):E1787-96. doi: 10.1073/pnas.1316599111. PubMed PMID: 24711394; PubMed Central PMCID: PMCPMC4035944.

18. Rotstein HG, Nadim F. Frequency preference in two-dimensional neural models: a linear analysis of the interaction between resonant and amplifying currents. J Comput Neurosci. 2014;37(1):9-28. doi: 10.1007/s10827-013-0483-3. PubMed PMID: 24254440; PubMed Central PMCID: PMCPMC4028432.

19. Rotstein HG. Subthreshold amplitude and phase resonance in models of quadratic type: nonlinear effects generated by the interplay of resonant and amplifying currents. J Comput Neurosci. 2015;38(2):325-54. doi: 10.1007/s10827-014-0544-2. PubMed PMID: 25586875.

20. Rotstein HG. Frequency Preference Response to Oscillatory Inputs in Two-dimensional Neural Models: A Geometric Approach to Subthreshold Amplitude and Phase Resonance. J Math Neurosci. 2014;4:11. doi: 10.1186/2190-8567-4-11. PubMed PMID: 24872925; PubMed Central PMCID: PMCPMC4014472.

21. Hutcheon B, Miura RM, Yarom Y, Puil E. Low-threshold calcium current and resonance in thalamic neurons: a model of frequency preference. J Neurophysiol. 1994;71(2):583-94. PubMed PMID: 8176427.

22. Chen Y, Li X, Rotstein HG, Nadim F. Membrane potential resonance frequency directly influences network frequency through electrical coupling. J Neurophysiol. 2016:jn 00361 2016. doi: 10.1152/jn.00361.2016. PubMed PMID: 27385799.

23. Buzsaki G. Theta oscillations in the hippocampus. Neuron. 2002;33(3):325-40. PubMed PMID: 11832222.

24. Hu H, Vervaeke K, Graham LJ, Storm JF. Complementary theta resonance filtering by two spatially segregated mechanisms in CA1 hippocampal pyramidal neurons. J Neurosci. 2009;29(46):14472-83. doi: 10.1523/JNEUROSCI.0187-09.2009. PubMed PMID: 19923281.

25. Stark E, Eichler R, Roux L, Fujisawa S, Rotstein HG, Buzsaki G. Inhibition-induced theta resonance in cortical circuits. Neuron. 2013;80(5):1263-76. doi: 10.1016/j.neuron.2013.09.033. PubMed PMID: 24314731; PubMed Central PMCID: PMC3857586.

26. Narayanan R, Johnston D. Long-term potentiation in rat hippocampal neurons is accompanied by spatially widespread changes in intrinsic oscillatory dynamics and excitability. Neuron. 2007;56(6):1061-75. Epub 2007/12/21. doi: 10.1016/j.neuron.2007.10.033. PubMed PMID: 18093527; PubMed Central PMCID: PMCPMC2430016.

27. Moca VV, Nikolic D, Singer W, Muresan RC. Membrane resonance enables stable and robust gamma oscillations. Cereb Cortex. 2014;24(1):119-42. doi: 10.1093/cercor/bhs293. PubMed PMID: 23042733; PubMed Central PMCID: PMCPMC3862267.

28. Tikidji-Hamburyan RA, Martinez JJ, White JA, Canavier CC. Resonant Interneurons Can Increase Robustness of Gamma Oscillations. J Neurosci. 2015;35(47):15682-95. doi: 10.1523/JNEUROSCI.2601-15.2015. PubMed PMID: 26609160; PubMed Central PMCID: PMCPMC4659828.

29. Marder E, Bucher D. Understanding circuit dynamics using the stomatogastric nervous system of lobsters and crabs. Annu Rev Physiol. 2007;69:291-316. doi: 10.1146/annurev.physiol.69.031905.161516. PubMed PMID: 17009928.

30. Marder E. Variability, compensation, and modulation in neurons and circuits. Proceedings of the National Academy of Sciences of the United States of America. 2011;108 Suppl 3:15542-8. doi: 10.1073/pnas.1010674108. PubMed PMID: 21383190; PubMed Central PMCID: PMC3176600.

31. Puil E, Gimbarzevsky B, Miura RM. Quantification of membrane properties of trigeminal root ganglion neurons in guinea pigs. J Neurophysiol. 1986;55(5):995-1016. PubMed PMID: 3711977.

32. Gutfreund Y, Yarom Y, Segev I. Subthreshold oscillations and resonant frequency in guinea-pig cortical neurons: physiology and modelling. J Physiol. 1995;483 (Pt 3):621-40. PubMed PMID: 7776248; PubMed Central PMCID: PMCPMC1157807.
33. Hutcheon B, Miura RM, Puil E. Subthreshold membrane resonance in neocortical neurons. J Neurophysiol. 1996;76(2):683-97. PubMed PMID: 8871191.
34. Hodgkin AL, Huxley AF. A quantitative description of membrane current and its application to conduction and excitation in nerve. J Physiol. 1952;117(4):500-44. PubMed PMID: 12991237; PubMed Central PMCID: PMCPMC1392413.
35. Golowasch J, Abbott LF, Marder E. Activity-dependent regulation of potassium currents in an identified neuron of the stomatogastric ganglion of the crab Cancer borealis. J Neurosci. 1999;19(20):RC33. Epub 1999/10/12. PubMed PMID: 10516335.
36. Khorkova O, Golowasch J. Neuromodulators, not activity, control coordinated expression of ionic currents. J Neurosci. 2007;27(32):8709-18. Epub 2007/08/10. doi: 27/32/8709 [pii]

10.1523/JNEUROSCI.1274-07.2007. PubMed PMID: 17687048.
37. Schulz DJ, Goaillard JM, Marder E. Variable channel expression in identified single and electrically coupled neurons in different animals. Nat Neurosci. 2006;9(3):356-62. doi: 10.1038/nn1639. PubMed PMID: 16444270.
38. Deb K. Multi-objective optimization using evolutionary algorithms. 1st ed. Chichester ; New York: John Wiley & Sons; 2001. xix, 497 p. p.
39. Rathour RK, Malik R, Narayanan R. Transient potassium channels augment degeneracy in hippocampal active dendritic spectral tuning. Sci Rep. 2016;6:24678. doi: 10.1038/srep24678. PubMed PMID: 27094086; PubMed Central PMCID: PMCPMC4837398.
40. Prinz AA, Bucher D, Marder E. Similar network activity from disparate circuit parameters. Nat Neurosci. 2004;7(12):1345-52. doi: 10.1038/nn1352. PubMed PMID: 15558066.
41. Zhao S, Golowasch J. Ionic current correlations underlie the global tuning of large numbers of neuronal activity attributes. J Neurosci. 2012;32(39):13380-8. doi: 10.1523/JNEUROSCI.6500-11.2012. PubMed PMID: 23015428; PubMed Central PMCID: PMCPMC3541048.
42. Schulz DJ, Goaillard JM, Marder EE. Quantitative expression profiling of identified neurons reveals cell-specific constraints on highly variable levels of gene expression. Proceedings of the National Academy of Sciences of the United States of America. 2007;104(32):13187-91. doi: 10.1073/pnas.0705827104. PubMed PMID: 17652510; PubMed Central PMCID: PMCPMC1933263.
43. Rotstein HG, Olarinre M, Golowasch J. Dynamic compensation mechanism gives rise to period and duty-cycle level sets in oscillatory neuronal models. J Neurophysiol. 2016;116(5):2431-52. doi: 10.1152/jn.00357.2016. PubMed PMID: 27559141.
44. Buchholtz F, Golowasch J, Epstein IR, Marder E. Mathematical model of an identified stomatogastric ganglion neuron. J Neurophysiol. 1992;67(2):332-40. PubMed PMID: 1373763.
45. Peck JH, Gaier E, Stevens E, Repicky S, Harris-Warrick RM. Amine modulation of Ih in a small neural network. J Neurophysiol. 2006;96(6):2931-40. doi: 10.1152/jn.00423.2005. PubMed PMID: 16943317.
46. Wang XJ. Neurophysiological and computational principles of cortical rhythms in cognition. Physiol Rev. 2010;90(3):1195-268. doi: 10.1152/physrev.00035.2008. PubMed PMID: 20664082; PubMed Central PMCID: PMCPMC2923921.
47. Engel TA, Schimansky-Geier L, Herz AV, Schreiber S, Erchova I. Subthreshold membrane-potential resonances shape spike-train patterns in the entorhinal cortex. J Neurophysiol. 2008;100(3):1576-89. doi: 10.1152/jn.01282.2007. PubMed PMID: 18450582; PubMed Central PMCID: PMC2544463.

779 48. Rotstein HG. Resonance modulation, annihilation and generation of antiresonance and
780 antiphasonance in 3D neuronal systems: interplay of resonant and amplifying currents with slow
781 dynamics. bioaRxiv 2016;091207. PubMed PMID: 091207.
782 49. Prinz AA, Billimoria CP, Marder E. Alternative to hand-tuning conductance-based models:
783 construction and analysis of databases of model neurons. J Neurophysiol. 2003;90(6):3998-4015. Epub
784 2003/08/29. doi: 10.1152/jn.00641.2003

785 00641.2003 [pii]. PubMed PMID: 12944532.
786 50. Haas JS, White JA. Frequency selectivity of layer II stellate cells in the medial entorhinal cortex. J
787 Neurophysiol. 2002;88(5):2422-9. doi: 10.1152/jn.00598.2002. PubMed PMID: 12424283.
788 51. Taylor AL, Goaillard JM, Marder E. How multiple conductances determine electrophysiological
789 properties in a multicompartment model. J Neurosci. 2009;29(17):5573-86. doi:
790 10.1523/JNEUROSCI.4438-08.2009. PubMed PMID: 19403824; PubMed Central PMCID: PMC2821064.
791 52. Johnson BR, Kloppenburg P, Harris-Warrick RM. Dopamine modulation of calcium currents in
792 pyloric neurons of the lobster stomatogastric ganglion. J Neurophysiol. 2003;90(2):631-43. Epub
793 2003/08/09. doi: 10.1152/jn.00037.2003

794 90/2/631 [pii]. PubMed PMID: 12904487.
795 53. Bucher D, Prinz AA, Marder E. Animal-to-animal variability in motor pattern production in adults
796 and during growth. J Neurosci. 2005;25(7):1611-9. PubMed PMID: 15716396.
797 54. Golowasch J. Ionic Current Variability and Functional Stability in the Nervous System. Bioscience.
798 2014;64(7):570-80. doi: 10.1093/biosci/biu070. PubMed PMID: 26069342; PubMed Central PMCID:
799 PMCPMC4460997.
800 55. Gimbarzevsky B, Miura RM, Puil E. Impedance profiles of peripheral and central neurons. Can J
801 Physiol Pharmacol. 1984;62(4):460-2. PubMed PMID: 6733594.
802 56. Mitchell M. An introduction to genetic algorithms. Cambridge, Mass.: MIT Press; 1996. viii, 205
803 p. p.
804 57. Malik A, Shim K, Prinz A, Smolinski T, G. Multi-objective evolutionary algorithms for analysis of
805 conductance correlations involved in recovery of bursting after neuromodulator deprivation in lobster
806 stomatogastric neuron models. BMC Neurosci. 2014;15(Suppl 1):P370.
807 58. Deb K, Pratap A, Agarwal S, Meyarivan T. A fast and elitist multiobjective genetic algorithm:
808 NSGA-II. IEEE Transactions on Evolutionary Computation. 2002;6(2):182-97. doi: 10.1109/4235.996017.
809 PubMed PMID: WOS:000175082800006.
810 59. Nowotny T, Levi R, Selverston AI. Probing the dynamics of identified neurons with a data-driven
811 modeling approach. PLoS One. 2008;3(7):e2627. doi: 10.1371/journal.pone.0002627. PubMed PMID:
812 18612435; PubMed Central PMCID: PMC2440808.
813 60. Burden RL, Faires JD. Numerical Analysis: PWS Publishing Company - Boston; 1980.
814 61. Ballo AW, Nadim F, Bucher D. Dopamine modulation of I_h improves temporal fidelity of spike
815 propagation in an unmyelinated axon. J Neurosci. 2012;32(15):5106-19. doi: 10.1523/JNEUROSCI.6320-
816 11.2012. PubMed PMID: 22496556; PubMed Central PMCID: PMCPMC3347488.

817

Supporting Information Legends

S1. Changing the value of $V_{1/2}^{H_\infty^m}$ does not change the correlations observed among the model parameters. a. Correlations shown in Fig. 8b with $V_{1/2}^{H_\infty^m}$ at -70 mV. **b.** Correlations obtained with $V_{1/2}^{H_\infty^m}$ set to -96 mV (red dots). MOEA was run only once in this case, compared to 5 times in panel a (hence the difference in the number of points). Black dots are the same as panel **a**. Note that the values of $\bar{g}_H$ in this case are about 10 times larger than those in panel **a**, but the correlations (green boxes) remain intact. More importantly, the range of parameters other than $\bar{g}_H$ is exactly the same in both cases.

S2. I_H extends the dynamic range of I_{Ca} parameters over which I_{Ca}-mediated MPR occurs. Parameter values for the optimal models in $\bar{g}_{Ca}$ - $V_{1/2}^{Ca_\infty^h}$ space shown for all models (grey dots) and those without I_H (blue dots). We removed I_H by setting $\bar{g}_H$ = 0, and ran the MOEA multiple times using the same Z- and φ-profiles to constrain the I_{Ca} parameters. A linear fit (green) shows that, when $\bar{g}_H$=0, the relationship between $\bar{g}_{Ca}$ - $V_{1/2}^{Ca_\infty^h}$ is linear and matches a narrow range of the high $\bar{g}_{Ca}$ values in fig 8c.

Figure Legends

Fig 1. Characterization of impedance amplitude *Z*(*f*) and phase *φ*(*f*) into target objective functions was performed to constrain the model parameters. The individual objective functions which collectively measure goodness-of-fit were taken as the distance away from characteristic points along the *Z*(*f*) and *φ*(*f*) profiles (green circles). **a.** The attributes used along *Z*(*f*) were Z_0=*Z*(f_0) at f_0=0.1 Hz, *Z*(f_1) at f_1 = 4 Hz, maximum impedance Z_{max}=*Z*(f_{res}) and the two points of the profile at $Z_0+Q_Z/2$. $Q_Z=Z_{max}-Z_0$. $\Lambda_{½}$ is the width of the profile at $Z_0+Q_Z/2$. **b.** The attributes used along *φ*(*f*) were *φ*(f_0), maximum advance φ_{max}, zero-phase frequency $f_{\varphi=0}$, $\varphi_{f=2}$ at 2 Hz and maximum delay φ_{min}.

Fig 2. Linear fits used to assess the sensitivity of impedance attributes on changes in parameters. Each model parameter was changed from the optimal value (origin) in both directions on a logarithmic scale to characterize parameter sensitivity. The slope of a linear fit of the relative change in the *Z*(*f*) attribute and the parameter was measured as sensitivity. The parameter was changed until the fit was no longer linear (R^2<0.98).

Fig 3. Membrane potential resonance MPR of the PD neuron was measured in voltage clamp. a. During ongoing activity, the PD neuron shows a slow-wave voltage waveform ranging approximately between -

60 and -30 mV. **b.** The membrane potential (V_{zap}) and the injected current (I_{PD}) were recorded when the PD neuron was voltage-clamped using a ZAP function between -60 and -30mV and sweeping frequencies between 0.1 and 4 Hz. The arrowhead indicates resonance, where the current amplitude is minimal and Z is maximal. **c.** The impedance amplitude $Z(f)$ (**c1**) and phase $\varphi(f)$ (**c2**) profiles of the PD neuron recorded in 18 preparations. The cross bars show the mean and SEM of f_{res} and Z_{max} (**c1**) and $f_{\varphi=0}$ (**c2**). The shaded region indicates the 95% confidence interval. **d.** The range of three $Z(f)$ attributes $f_{res,}$ Q_Z, and $\Lambda_{1/2}$ and one $\varphi(f)$ attribute $f_{\varphi=0}$. Each attribute was normalized to the median of its distribution for cross comparison. CoV is the coefficient of variation.

Fig. 4. Optimal models were fit to the impedance attributes of a single PD neuron. The $Z(f)$ (**a**) and $\varphi(f)$ (**b**) profiles of 500 randomly selected models from the optimal dataset (light blue curves) are compared to the target neuron's impedance profiles (red circles). All attributes (except φ_{max}) were captured to within 5% accuracy. The values of the biological target impedance amplitude attributes (in Hz, MΩ) were: (f_0, Z_0) = (0.1, 8.2), (f_{res}, Z_{max}) = (1, 13.7), (0.4, 11.65), (2.5, 11.65) and (4, 9.6). The target impedance phase attributes (in Hz, rad) were: (0.1, 0), ($f_{\varphi max}$, φ_{max}) = (0.4, 0.5), ($f_{\varphi=0}$, 0) = (1.05, 0), (2, -4), ($f_{\varphi min}$, φ_{min}) = (4, -0.4).

Fig 5. Passive and voltage-gated currents contribute to the generation of MPR. a. $Z(f)$ for a random model from the optimal dataset. We measured the steady-state response to sinusoidal voltage inputs (inset) at 0.1 Hz, f_{res}=1 Hz, and 4 Hz. Voltage-gated (I_{Ca} and I_H) and passive currents (I_L + I_{Cm}) are plotted as a function of voltage (left) and normalized time or cycle phase (right) at 0.1 Hz (**b**), 1 Hz (**c**), and 4Hz (**d**). The inset in **5c** shows one standard deviation around the mean for the data shown in the right panel, calculated for 200 randomly selected models.

Fig 6. f_{res} and $f_{\phi=0}$ of the optimal models are nearly identical. a. $Z(f)$ (top) and $\varphi(f)$ (bottom) for a representative optimal model. Green dots indicate f_{res} (top) and $f_{\phi=0}$ (bottom). **b.** Histogram showing the difference between f_{res} and $f_{\phi=0}$ for 500 randomly selected models. A comparison of f_{res} and $f_{\phi=0}$ of the experimental data of the PD neuron shows a similar distribution (inset, N=18). **(c)** Plots of steady-state responses of I_{Ca}, I_L, and I_{total} to sinusoidal voltage inputs at the frequencies marked in panel **a** shown as a function of normalized time (cycle phase). Dotted vertical line indicates cycle phase 0.5 where the passive currents peak. Solid lines connect the minimum of I_{Ca} to the peak of I_{total}. The two lines nearly align at $f_{\phi=0}$.

Fig 7. The time constants of I_{Ca} activation and inactivation control f_{res} and Z_{max}. The $Z(f)$ profiles are plotted for a randomly selected optimal model (green) at different values of τ_m^{Ca} (**a**) and τ_h^{Ca} (**b**). Note that f_{res} of the control (100%) values are at 1 Hz (dashed vertical line). The currents I_{Ca}, I_L and I_{total} plotted as a function of cycle phase at 50% (**c1**, **d1**), 100% (**c2**, **d2**), and 150% (**c3**, **d3**) of the control values of τ_m^{Ca} (**c**) and τ_h^{Ca} (**d**). In each panel of c and d, the currents are shown at 1 Hz (along the dashed lines in **a**, **b**) and at f_{res} (filled circles in **a**, **b**).

Fig 8. The optimal models show variability in individual and pairs of parameters. a. The range of parameters for all optimal models (~9000). Each parameter is normalized by its median value for cross comparison. The median values were $\bar{g}_L = 0.096\mu S$, $\bar{g}_H = 0.164\mu S$, $\bar{g}_{Ca} = 0.172\mu S$, $\tau_m^h = 2179ms$, $V_{1/2}^{Ca_m^\infty} = -51mV$, $\tau_m^{Ca} = 70ms$, $V_{1/2}^{Ca_h^\infty} = -67mV$, $\tau_h^{Ca} = 458ms$. Three representative optimal model parameter sets are shown (cyan, orange, purple solid line segments) indicating that widely different parameter combinations can produce the biological $Z(f)$ and $\varphi(f)$. CoV is coefficient of variation. **b.** Pairwise relationships among parameters of all optimal models (black dots). The range of parameter space was sampled within the prescribed limits given to the optimization routine, shown by including the sampled non-optimal models (grey). Permutation test showed significant pairwise correlations (green highlighted boxes with linear fits shown as green lines). **c.** Optimal models could be separated into two highly significant linear fits (green lines) in $\bar{g}_{Ca}$ - $V_{1/2}^{Ca_\infty^h}$ according to whether $\bar{g}_{Ca}$ < 0.05 (red; Low $\bar{g}_{Ca}$) or $\bar{g}_{Ca}$ > 0.05 (cyan; High $\bar{g}_{Ca}$). **d.** All pairwise relationships, separated on the low or high $\bar{g}_{Ca}$ (colors as in panel **c**). Green boxes are the same as in **b**.

Fig 9. The effect of the lower voltage bound V_{low} of oscillations on f_{res} and Z_{max} constrains the optimal models. a. An example of the change in $Z(f)$ measured in the biological PD neuron for V_{low} =-60mV (black line) and V_{low} =-70mV (grey line). Inset shows the bounds of voltage clamp inputs in the two cases. **b.** Shifting V_{low} from -60 mV to -70 mV lowers the value of f_{res} measured in the PD neuron significantly, without influencing Z_{max} (**b.** Experimental)**.** f_{res} and Z_{max} values measured in a random subset of optimal model neurons corresponding to low or high $\bar{g}_{Ca}$ values produced the same f_{res} and Z_{max} values at V_{low} = -60mV (black dots), but distinct f_{res} and Z_{max} values at V_{low} = -70mV (low $\bar{g}_{Ca}$: red dots; high $\bar{g}_{Ca}$: cyan dots). A subset of optimal models could reproduce the experimental result in which f_{res} shifted to significantly lower values without affecting Z_{max}. (grey dots). **(c)** $\bar{g}_{Ca}$ - $V_{1/2}^{Ca_\infty^h}$ relationship separating out the different groups of models producing different responses to changes in V_{low} (colors correspond to **b** Model panel). Models depicted by grey dots are referred to as intermediate $\bar{g}_{Ca}$ models. (**d1-e3**) mean voltage-gated ionic currents I_{Ca}, I_H and I_{Ca}+I_H and I_{total}, shown as a function of voltage for V_{low} =-60 mV (**d1-d3**) and

V_{low} = -70 mV (**e1-e3**). Numbers correspond to the location along the $\bar{g}_{Ca}$ - $V_{1/2}^{Ca_\infty^h}$ as shown in **c**. **f.** The intermediate $\bar{g}_{Ca}$ models (grey dots) show a distinct $\bar{g}_{Ca}$ - $V_{1/2}^{Ca_\infty^h}$ linear correlation. **g.** Intermediate $\bar{g}_{Ca}$ models (grey dots) show a distinct and tighter τ_m^{Ca} - τ_h^{Ca} correlation compared to all optimal models (black dots). **h.** Intermediate $\bar{g}_{Ca}$ models (grey dots) show a strong $\bar{g}_{Ca}$ - $\bar{g}_H$ linear correlation that is not observed for all optimal models (black dots).

Fig 10. Assessing the dependence of f_{res} and Q_Z on the τ_m^{Ca} - τ_h^{Ca} linear correlation. **a.** Parameter values for each model were changed along a line parallel (, blue) to the correlation line (black) or along a perpendicular line (⊥, grey). This was done for models with high (cyan; **a1**), low (red; **a2**) and intermediate (grey; **a3**) $\bar{g}_{Ca}$ models. For each model and each line, or ⊥, we fit a line to the relative change in either f_{res} or Q_Z as a function of the relative change in $\bar{g}_{Ca}$. **b.** The sensitivity values of f_{res} or Q_Z to or ⊥ are shown for the three groups. **c.** Impedance profiles showing how Q_Z changes when the parameters vary along a line parallel (blue) or perpendicular (grey) to the τ_m^{Ca} - τ_h^{Ca} correlation line in one optimal model. Arrows show the direction of the movement of Z_{max} and f_{res} for the change in parameters along or ⊥ for the high (**c1**), low (**c2**) and intermediate (**c3**) $\bar{g}_{Ca}$ model.

Fig 11. Assessing the dependence of f_{res} and Q_Z on the linear $\bar{g}_{Ca}$ - $V_{1/2}^{Ca_h^\infty}$ correlation. **a.** Parameter values for each model were changed along a line parallel (, blue) to the correlation line (black) or along a perpendicular line (⊥, grey). This was done for models with high (cyan; **a1**), low (red; **a2**) and intermediate (grey; **a3**) $\bar{g}_{Ca}$ models. For each model and each line, or ⊥, we fit a line to the relative change in either f_{res} or Q_Z as a function of the relative change in $\bar{g}_{Ca}$. **b.** The sensitivity values of f_{res} or Q_Z to or ⊥ are shown for the three groups. **c.** Impedance profiles showing how Q_Z changes when the parameters vary along a line parallel (blue) or perpendicular (grey) to the $\bar{g}_{Ca}$ - $V_{1/2}^{Ca_h^\infty}$ correlation line in one optimal model. Arrows show the direction of the movement of Z_{max} and f_{res} for the change in parameters along or ⊥ for the high (**c1**), low (**c2**) and intermediate (**c3**) $\bar{g}_{Ca}$ model.

Fig 12. Assessing the dependence of f_{res} and Q_Z of the intermediate $\bar{g}_{Ca}$ models on the linear $\bar{g}_{Ca}$ - $\bar{g}_H$ correlation. **a.** Parameter values for each model were in the intermediate $\bar{g}_{Ca}$ group (see fig 9) were changed along a line parallel (, blue) to the correlation line (black) or along a perpendicular line (⊥, grey). For each model and each line, or ⊥, we fit a line to the relative change in either f_{res} or Q_Z as a function of the relative change in $\bar{g}_{Ca}$. **b.** The sensitivity values of f_{res} or Q_Z to or ⊥ are shown for the three groups. **c.** Impedance profiles showing how Q_Z changes when the parameters vary along a line parallel (blue) or perpendicular (grey) to the $\bar{g}_{Ca}$ - $\bar{g}_H$ correlation line in one optimal model. Arrows show the direction of the movement of Z_{max} and f_{res} for the change in parameters along or ⊥.

Tables

	$\bar{g}_L$	$\bar{g}_H$	$\bar{g}_{Ca}$	τ_m^H	$V_{1/2}^{Ca_\infty^m}$	τ_m^{Ca}	$V_{1/2}^{Ca_\infty^h}$	τ_h^{Ca}
Low	0	0	0	0	-75	0	-75	0
High	0.15	0.35	0.35	3000	-30	100	-30	1000

Table 1. Limits of parameter values allowed for the PD neuron models. $V_{1/2}^{H_\infty^m}$ was fixed at -70 mV since there is little variability in the reporting of this experimental measurement [45, 61]. Voltages are in mV, maximal conductances in µS and time constants in ms.

	$\bar{g}_L$	$\bar{g}_H$	$\bar{g}_{Ca}$	τ_m^H	$V_{1/2}^{Ca_\infty^m}$	τ_m^{Ca}	$V_{1/2}^{Ca_\infty^h}$	τ_h^{Ca}
$\bar{g}_L$		0.003	0.358	0.147	0.272	0.002	0.347	< 0.001
$\bar{g}_H$	0.003		0.288	0.03	0.442	0.104	0.21	0.004
$\bar{g}_{Ca}$	0.349	0.046		0.449	0.512	0.485	<.001	0.129
τ_m^H	0.054	0.001	0.002		0.349	0.470	0.417	0.121
$V_{1/2}^{Ca_\infty^m}$	0.233	0.496	0.138	0.277		0.378	0.452	0.037
τ_m^{Ca}	0.133	0.510	0.191	0.253	0.05		0.318	0.036
$V_{1/2}^{Ca_\infty^h}$	0.368	0.07	<0.001	< 0.001	0.068	0.092		0.27
τ_h^{Ca}	0.307	0.452	0.008	0.05	< 0.001	< 0.001	0.001	

Table 2. Statistical p-values obtained using the permutation test of pairwise comparisons for low (lower triangle) and high (upper triangle) $\bar{g}_{Ca}$. Underlined values are statistically significant (p<0.05).

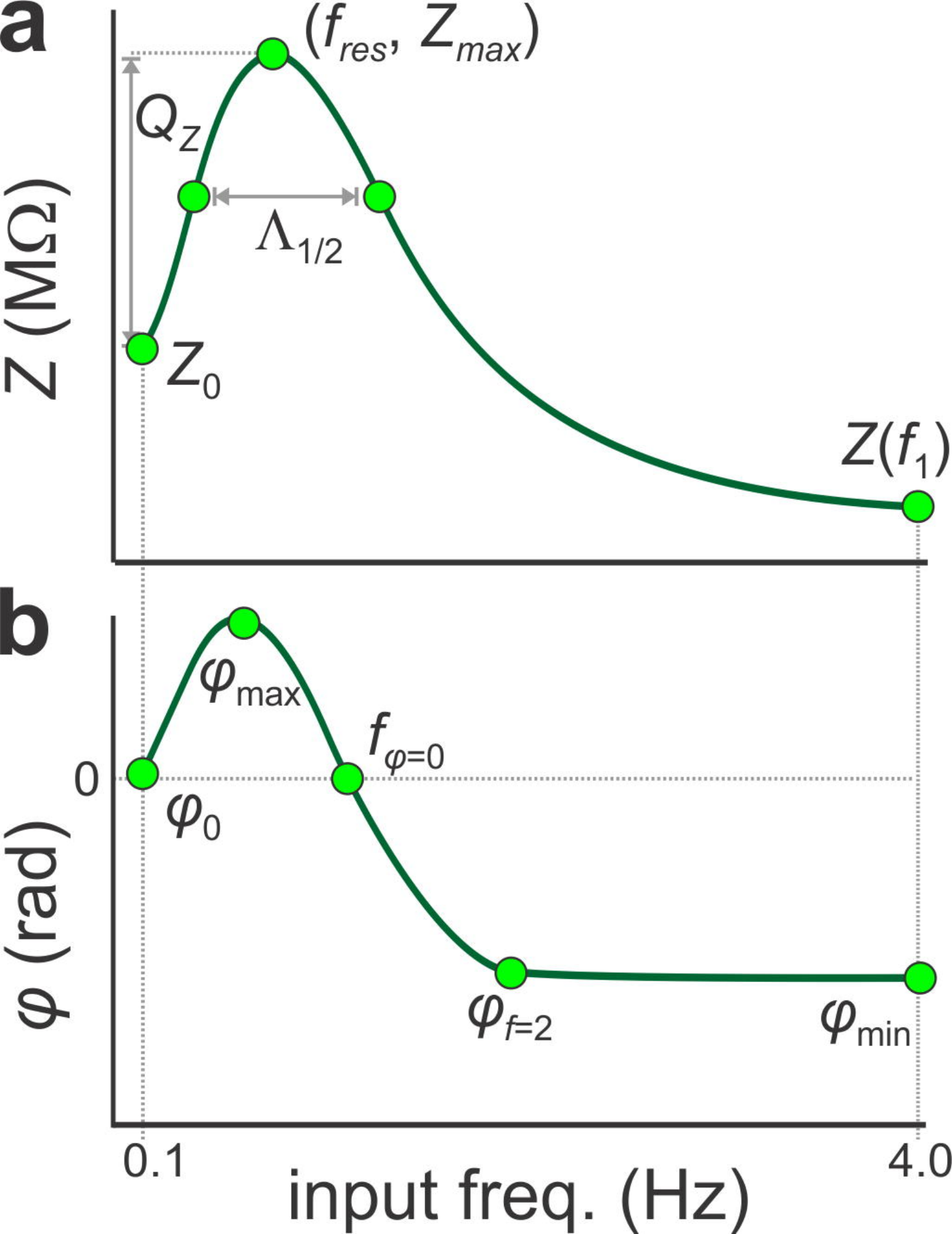
a
(f_{res}, Z_{max})
Q_Z
$\Lambda_{1/2}$
Z_0
$Z(f_1)$
Z (MΩ)
b
φ_{max}
$f_{\varphi=0}$
0
φ_0
$\varphi_{f=2}$
φ_{min}
φ (rad)
0.1
4.0
input freq. (Hz)

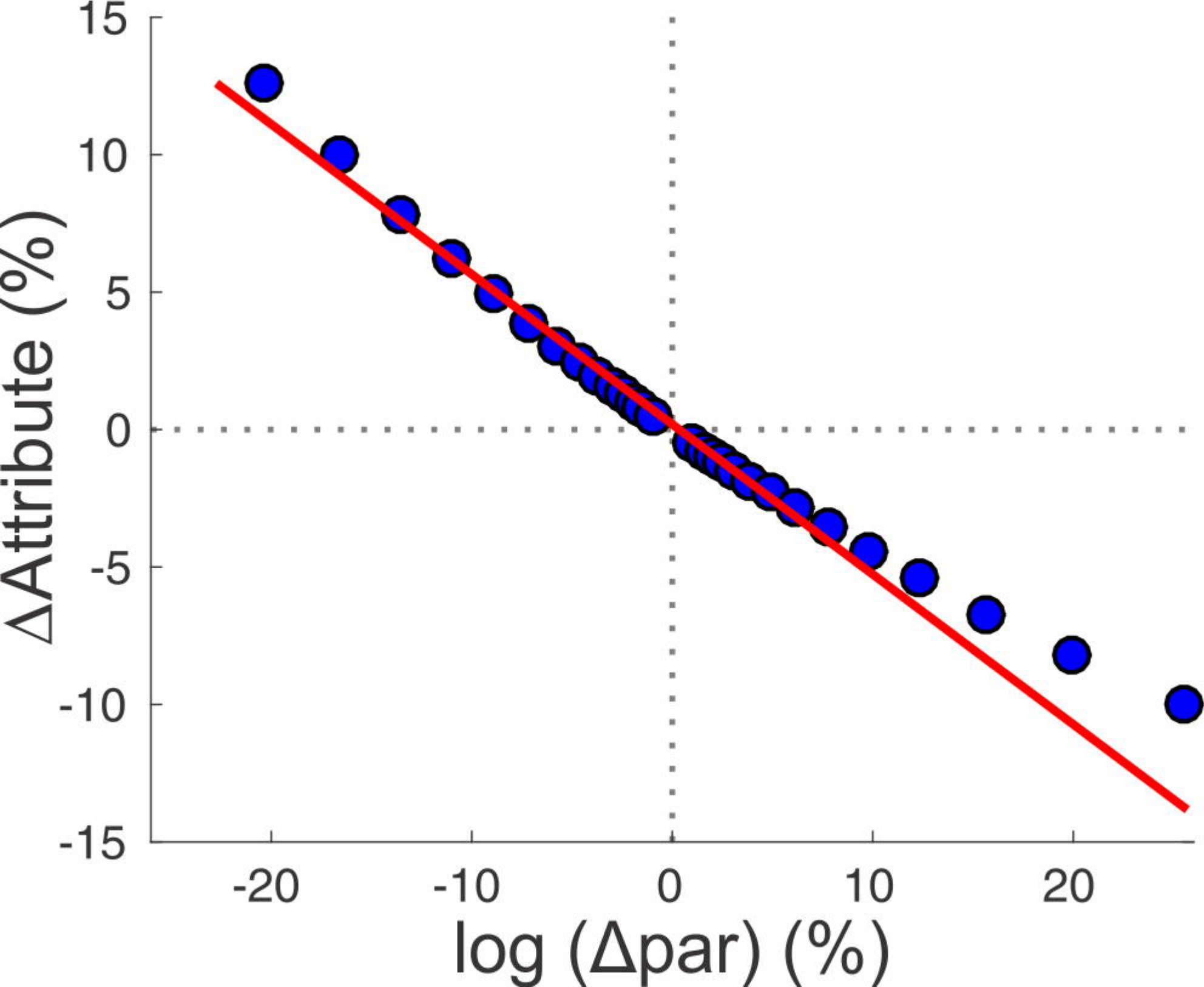
15
10
5
0
-5
-10
-15
ΔAttribute (%)
-20
-10
0
10
20
log (Δpar) (%)

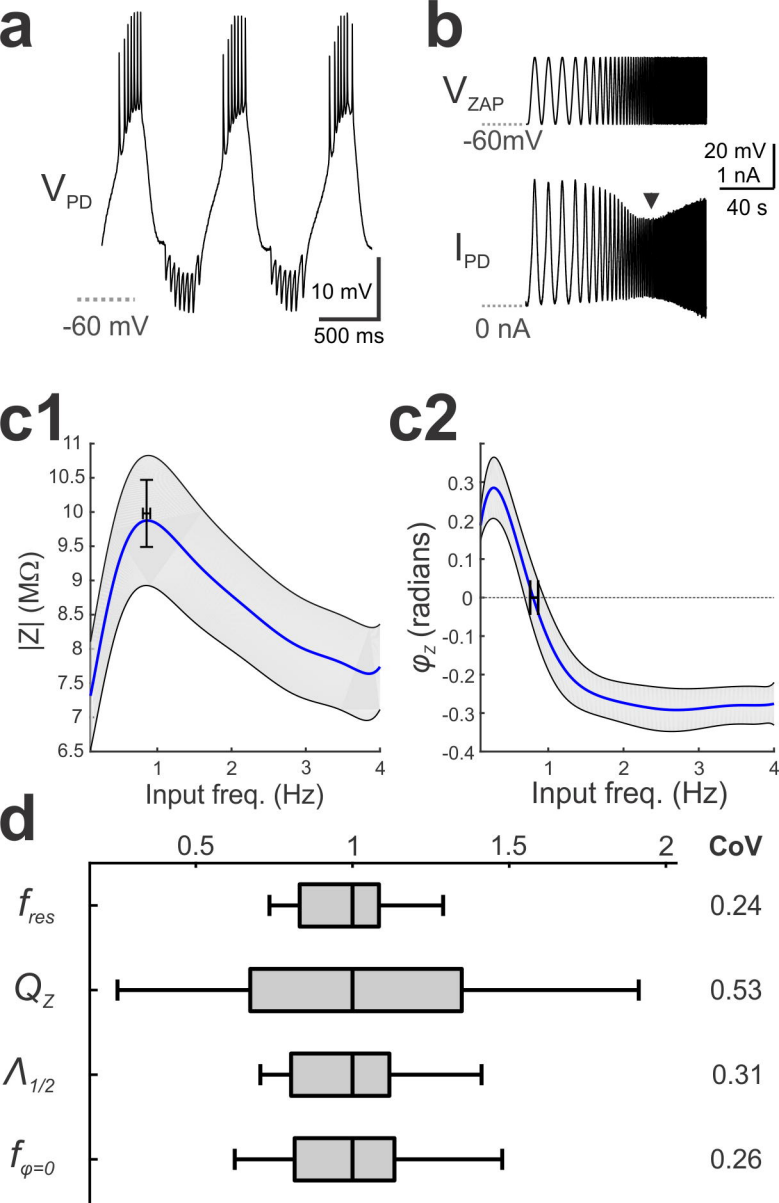
a
V_PD
-60 mV
10 mV
500 ms
b
V_ZAP
-60mV
20 mV
1 nA
40 s
I_PD
0 nA
c1
|Z| (MΩ)
Input freq. (Hz)
c2
φ_Z (radians)
Input freq. (Hz)
d
0.5
1
1.5
2
CoV
f_res
0.24
Q_Z
0.53
Λ_1/2
0.31
f_φ=0
0.26

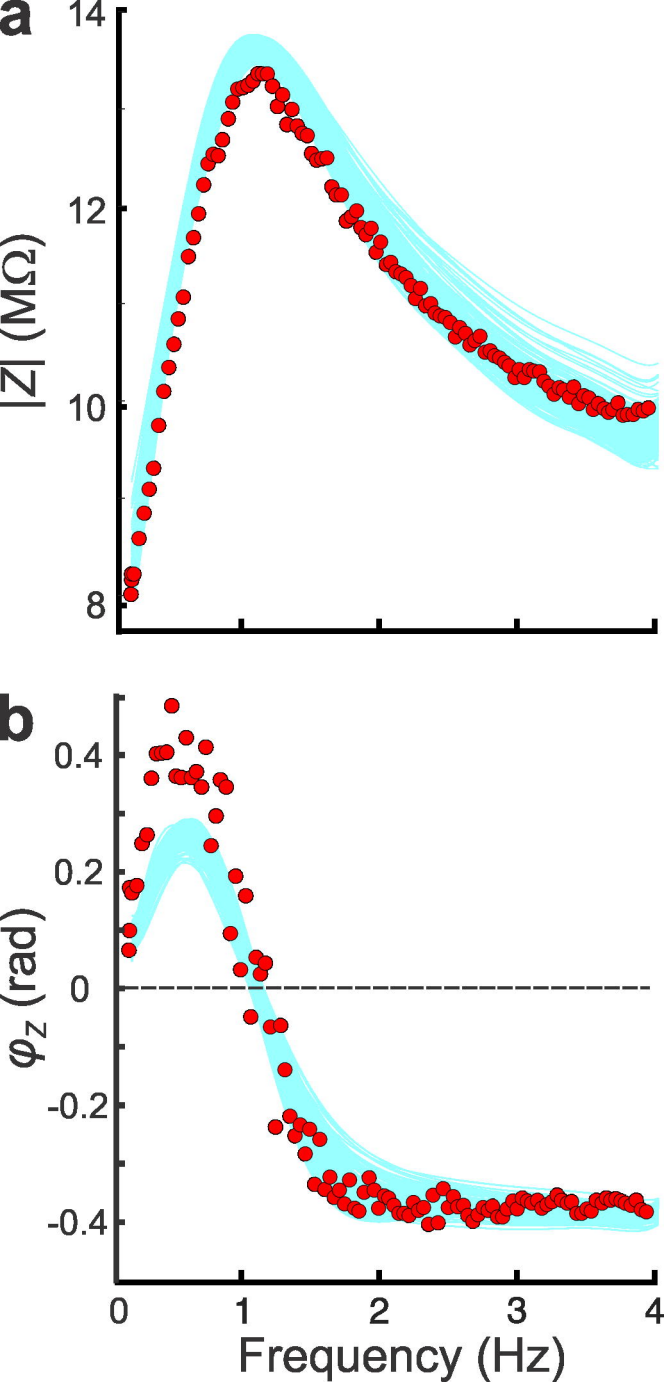
a
14
12
10
8
|Z| (MΩ)
b
0.4
0.2
0
-0.2
-0.4
φz (rad)
0
1
2
3
4
Frequency (Hz)

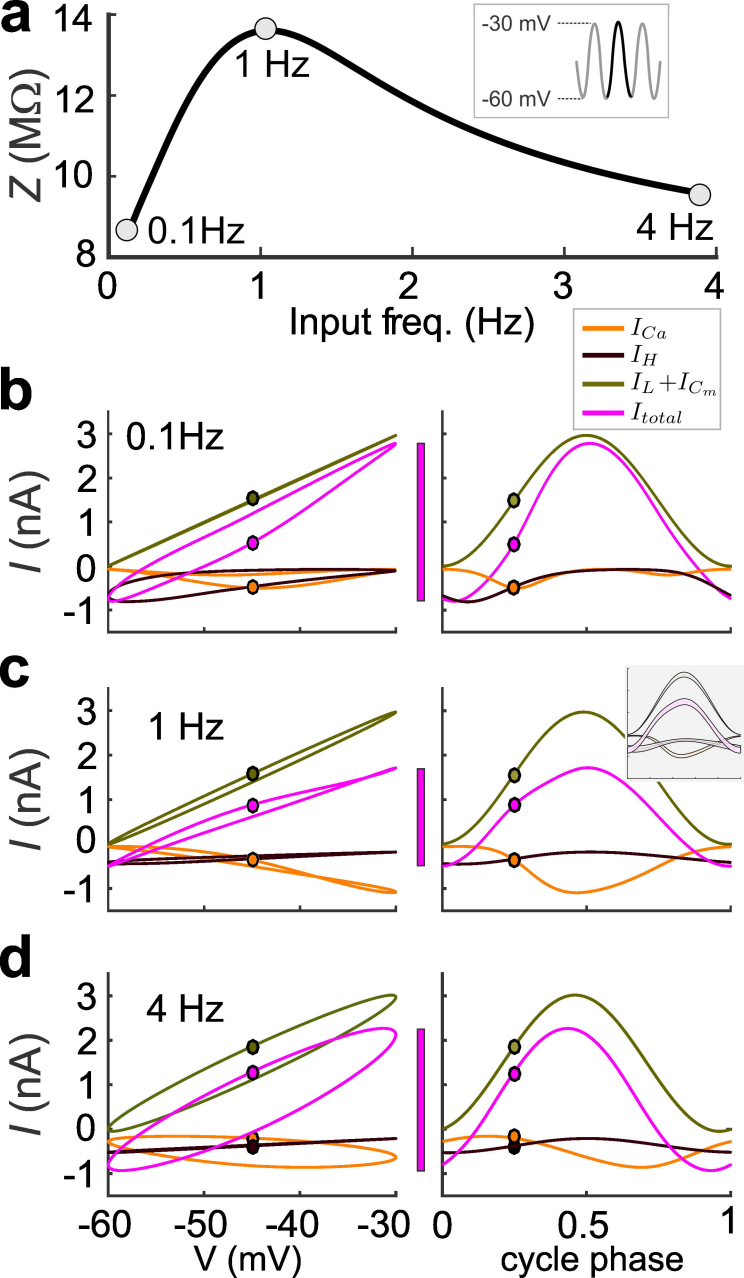
a
Z (MΩ)
Input freq. (Hz)
0.1Hz
1 Hz
4 Hz
-30 mV
-60 mV
I_{Ca}
I_H
$I_L+I_{C_m}$
I_{total}
b
0.1Hz
I (nA)
c
1 Hz
d
4 Hz
V (mV)
cycle phase

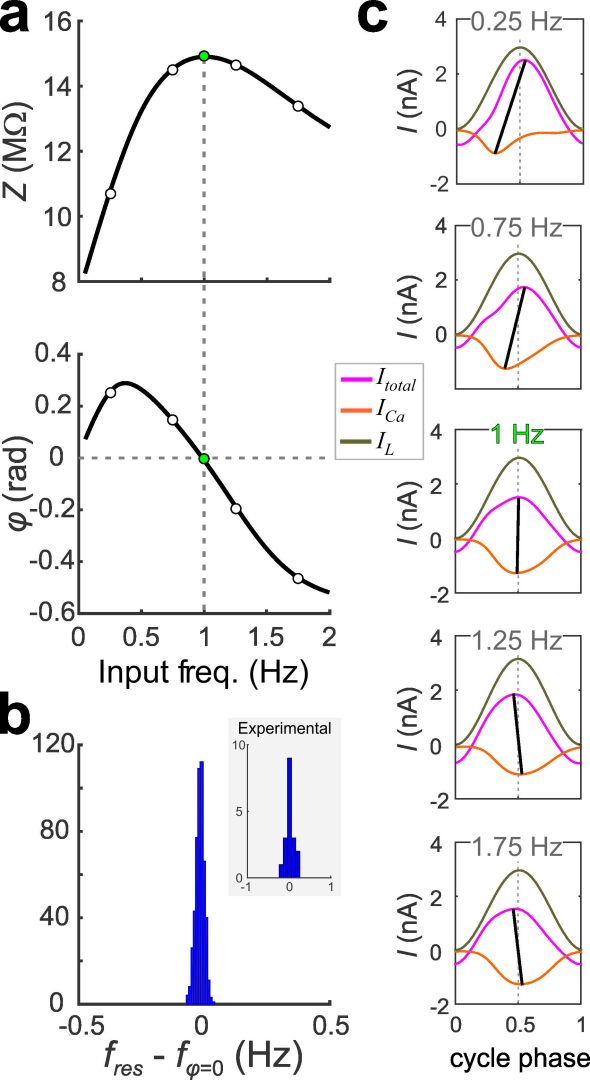
a
Z (MΩ)
φ (rad)
Input freq. (Hz)
I_{total}
I_{Ca}
I_L
b
Experimental
f_{res} - $f_{\varphi=0}$ (Hz)
c
0.25 Hz
0.75 Hz
1 Hz
1.25 Hz
1.75 Hz
I (nA)
cycle phase

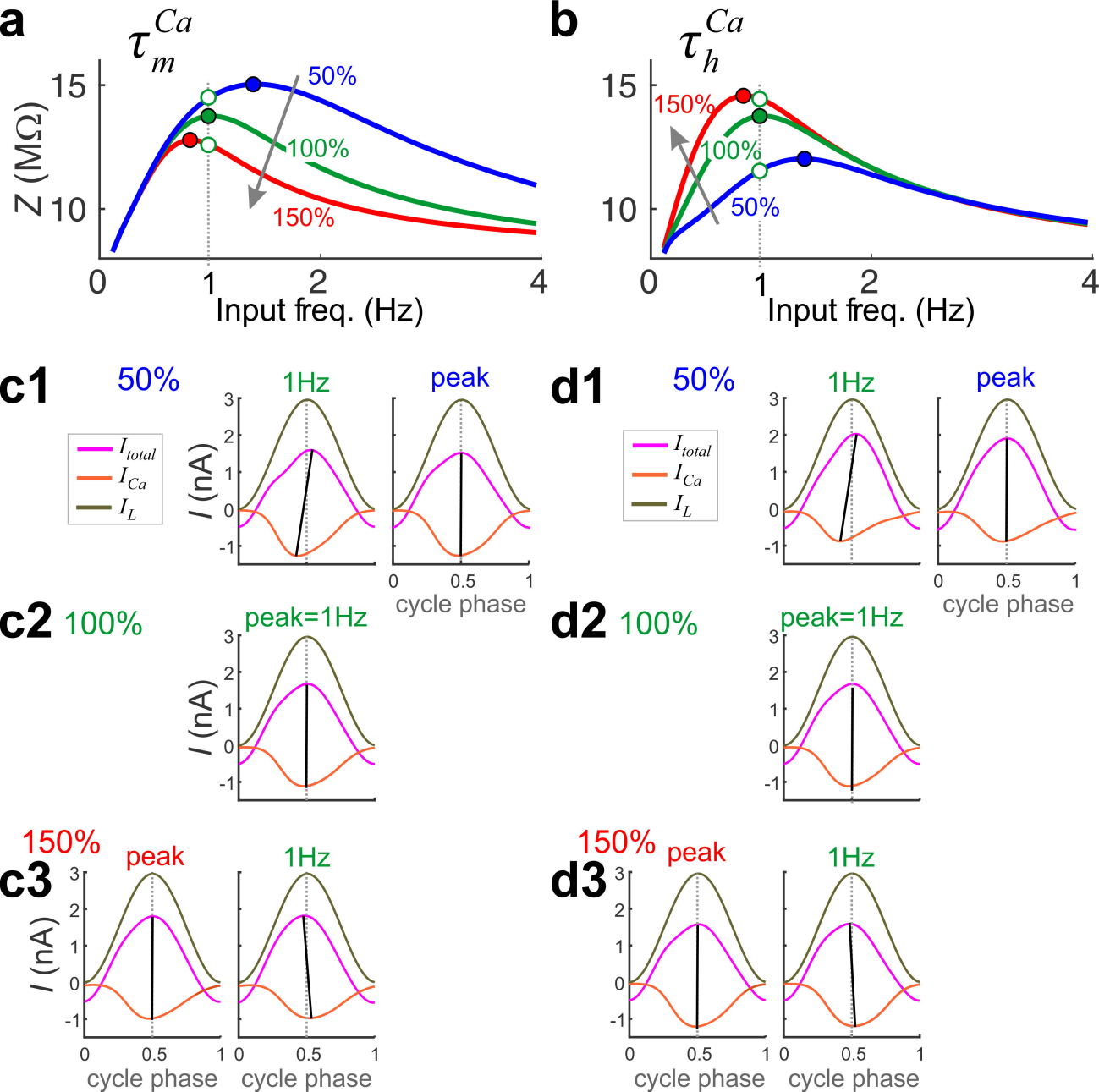
a
τ_m^{Ca}
50%
100%
150%
Z (MΩ)
15
10
0
1
2
4
Input freq. (Hz)
b
τ_h^{Ca}
150%
100%
50%
15
10
0
1
2
4
Input freq. (Hz)
c1
50%
1Hz
peak
I_{total}
I_{Ca}
I_L
I (nA)
3
2
1
0
-1
0
0.5
1
cycle phase
d1
50%
1Hz
peak
I_{total}
I_{Ca}
I_L
cycle phase
c2
100%
peak=1Hz
I (nA)
d2
100%
peak=1Hz
c3
150%
peak
1Hz
I (nA)
cycle phase
cycle phase
d3
150%
peak
1Hz
cycle phase
cycle phase

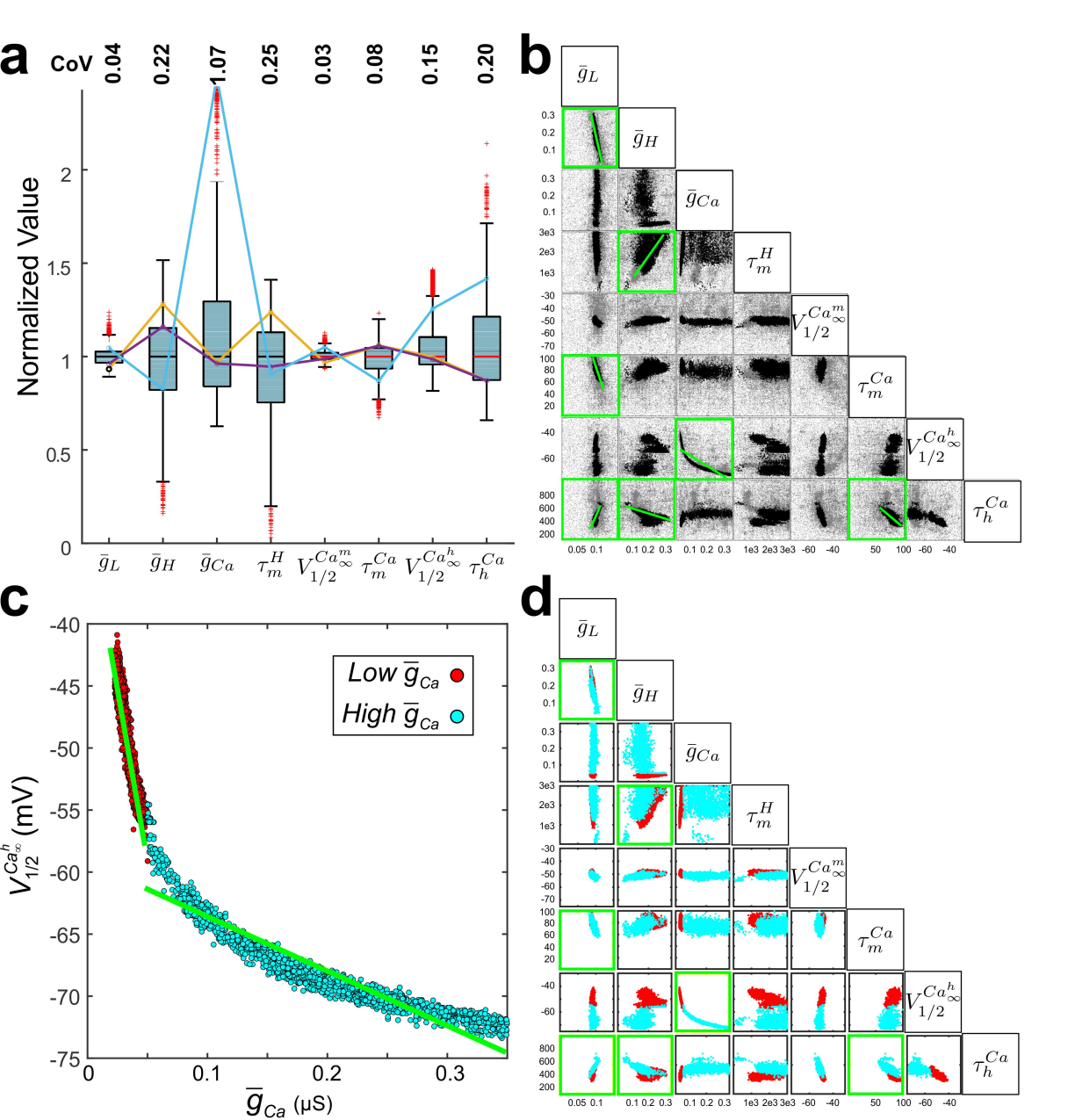
a
CoV
0.04
0.22
1.07
0.25
0.03
0.08
0.15
0.20
Normalized Value
$\bar{g}_L$
$\bar{g}_H$
$\bar{g}_{Ca}$
τ_m^H
$V_{1/2}^{Ca_\infty^m}$
τ_m^{Ca}
$V_{1/2}^{Ca_\infty^h}$
τ_h^{Ca}
b
c
Low $\bar{g}_{Ca}$
High $\bar{g}_{Ca}$
$V_{1/2}^{Ca_\infty^h}$ (mV)
$\bar{g}_{Ca}$ (μS)
d

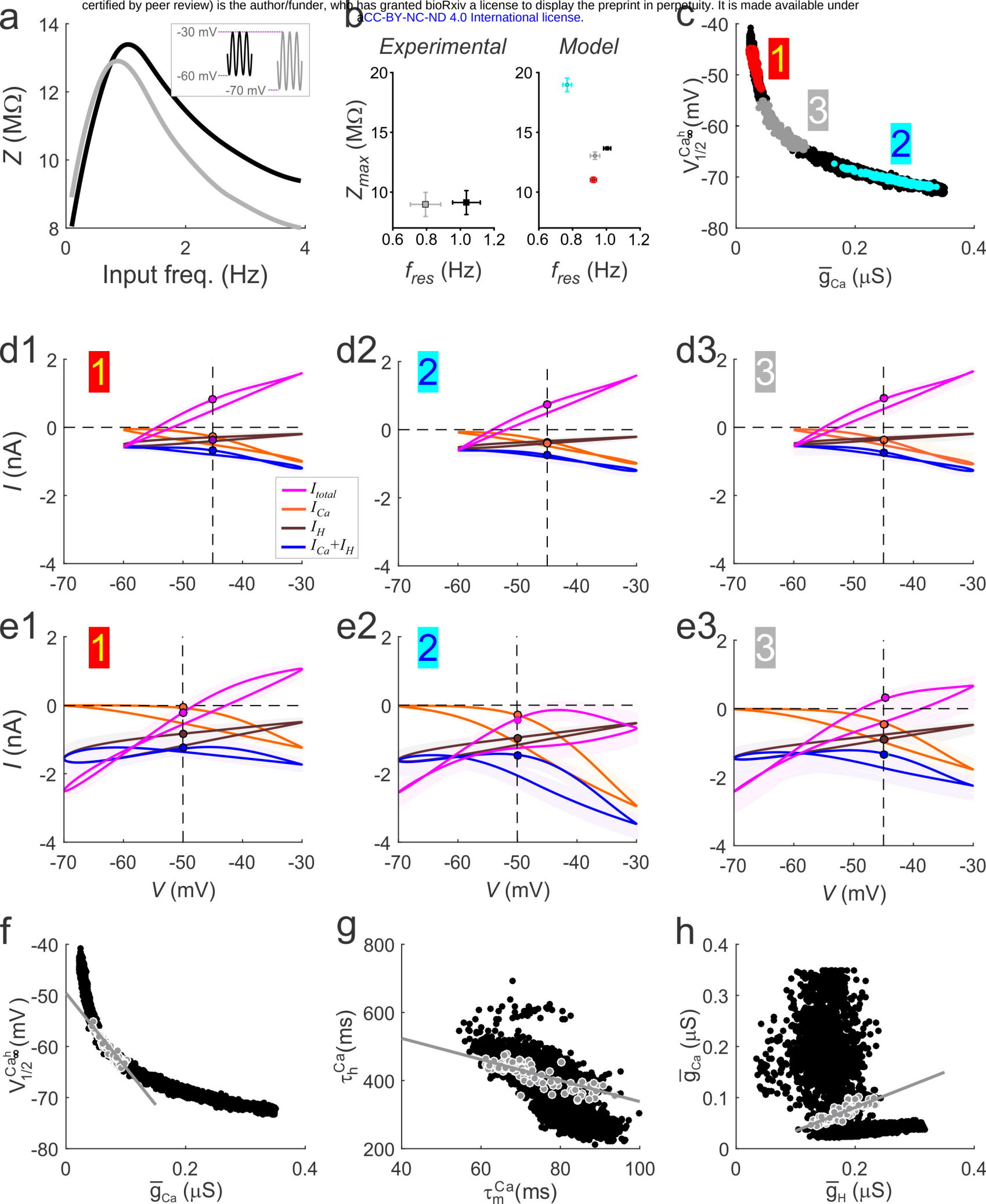

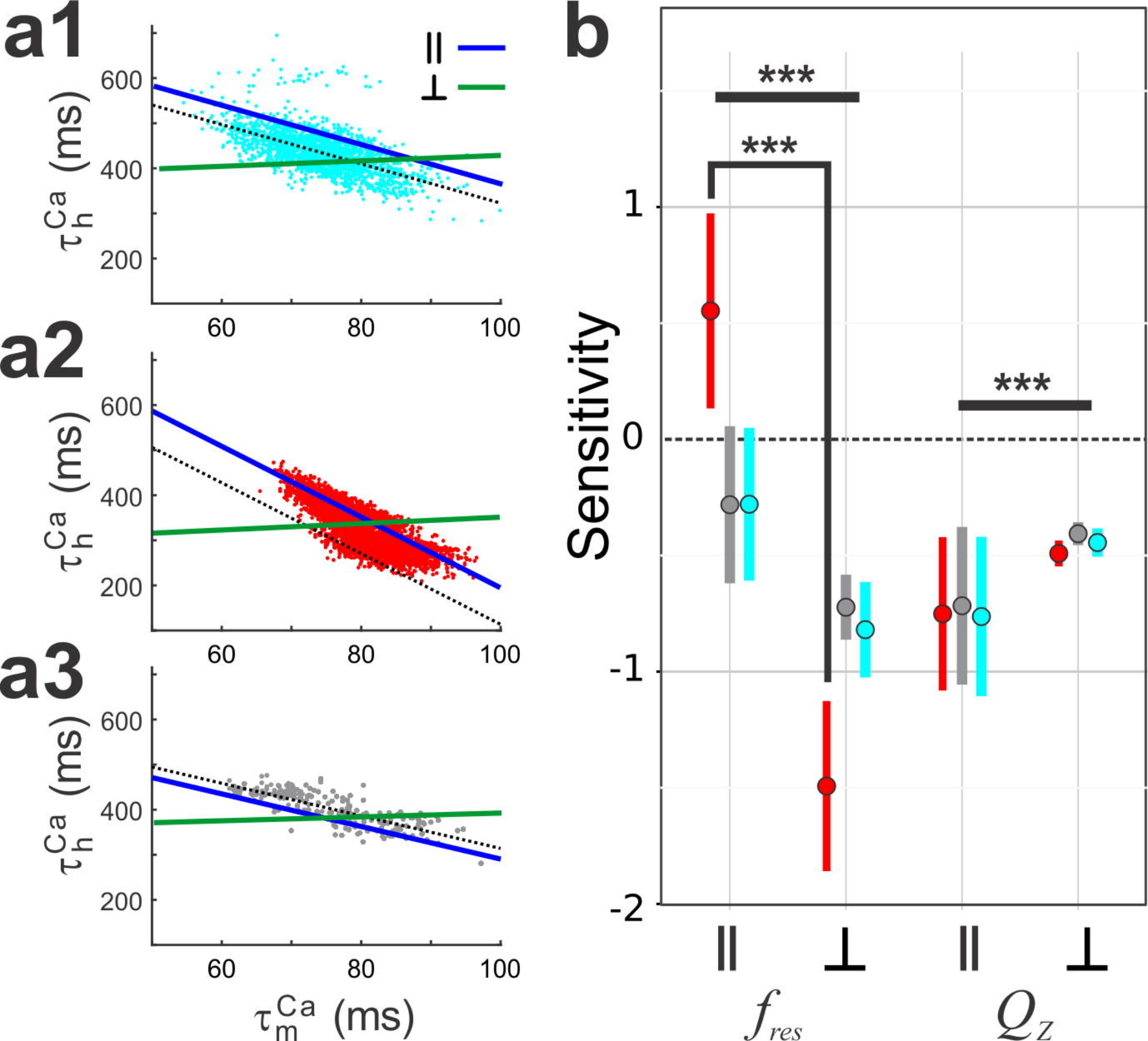
a1
a2
a3
b
∥
⊥
600
400
200
60
80
100
τ_h^{Ca} (ms)
τ_m^{Ca} (ms)
***
***
***
Sensitivity
1
0
-1
-2
f_{res}
Q_Z

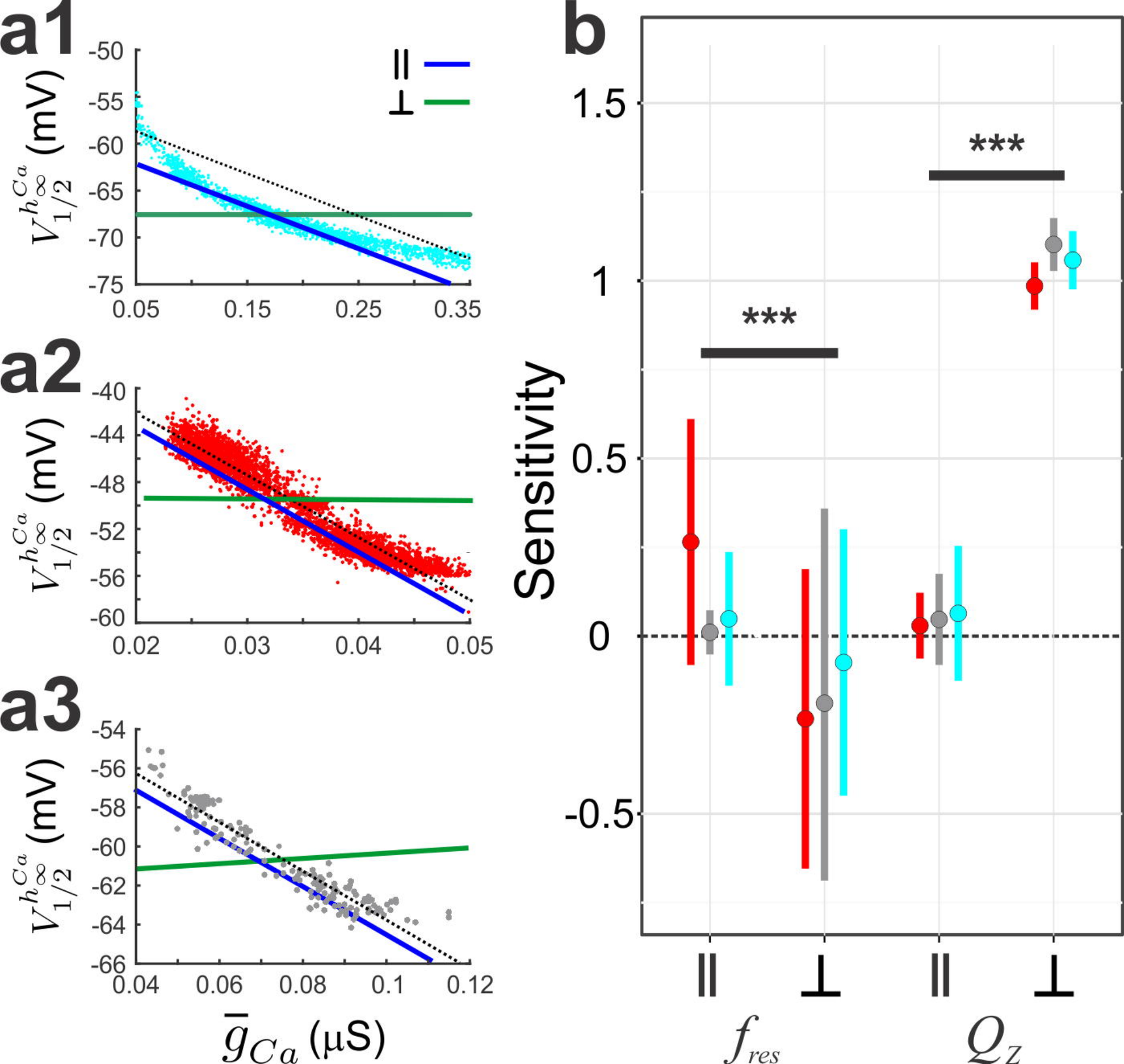
a1
a2
a3
b
$V_{1/2}^{h_\infty^{Ca}}$ (mV)
$\bar{g}_{Ca}$ (μS)
∥
⊥
Sensitivity
***
***
f_{res}
Q_Z

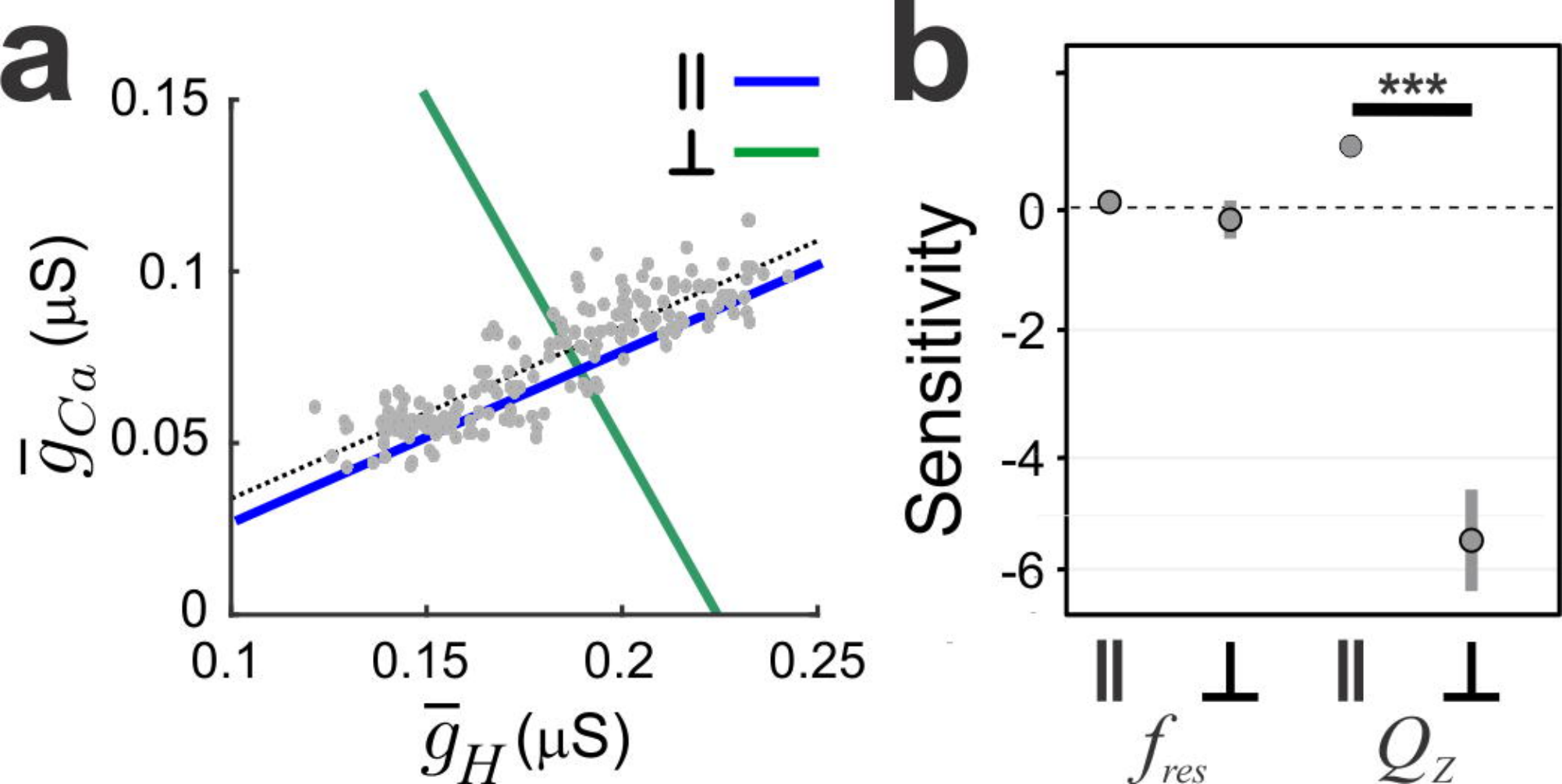
a
0.15
0.1
0.05
0
$\bar{g}_{Ca}$ (μS)
0.1
0.15
0.2
0.25
$\bar{g}_H$ (μS)
∥
⊥
b
***
Sensitivity
0
-2
-4
-6
∥
⊥
∥
⊥
f_{res}
Q_Z